WILEY

Publishers Since 1807

JOHN WILEY & SONS, LTD., THE ATRIUM, SOUTHERN GATE, CHICHESTER P019 8SQ, UK

*** PROOF OF YOUR ARTICLE ATTACHED, PLEASE READ CAREFULLY ***

After receipt of your corrections your article will be published initially within the online version of the journal.

PLEASE NOTE THAT THE PROMPT RETURN OF YOUR PROOF CORRECTIONS WILL ENSURE THAT THERE ARE NO UNNECESSARY DELAYS IN THE PUBLICATION OF YOUR ARTICLE

☐ **READ PROOFS CAREFULLY**

ONCE PUBLISHED ONLINE OR IN PRINT IT IS NOT POSSIBLE TO MAKE ANY FURTHER CORRECTIONS TO YOUR ARTICLE

- This will be your only chance to correct your proof
- Please note that the volume and page numbers shown on the proofs are for position only

☐ **ANSWER ALL QUERIES ON PROOFS** (Queries are attached as the last page of your proof.)

- List all corrections and send back via e-mail to the production contact as detailed in the covering e-mail, or mark all corrections directly on the proofs and send the scanned copy via e-mail. Please do not send corrections by fax or post

☐ **CHECK FIGURES AND TABLES CAREFULLY**

- Check sizes, numbering, and orientation of figures
- All images in the PDF are downsampled (reduced to lower resolution and file size) to facilitate Internet delivery. These images will appear at higher resolution and sharpness in the printed article
- Review figure legends to ensure that they are complete
- Check all tables. Review layout, titles, and footnotes

☐ **COMPLETE COPYRIGHT TRANSFER AGREEMENT (CTA) if you have not already signed one**

- Please send a scanned signed copy with your proofs by e-mail. **Your article cannot be published unless we have received the signed CTA**

☐ **AUTHOR SERVICES**

- If you have registered this article in Wiley-Blackwell Author Services, the article's status will be updated shortly after you have returned your proof corrections (you will also receive an e-mail alert if you have opted to receive them). **You are entitled to free access to the PDF from Author Services when your article is published online**. This free access is considered your PDF offprint, and you will only have access from within Author Services; you will not be sent a PDF. You may also nominate up to 10 colleagues for free access. All accesses from Author Services count towards the usage of your article. For options to order print copies or additional electronic access, please see below.

☐ **OFFPRINTS**

- Free access to the final PDF offprint of your article will be available via Author Services only. Please therefore sign up for Author Services if you would like to access your article PDF offprint and enjoy the many other benefits the service offers

Additional reprint and journal issue purchases

- Should you wish to purchase a minimum of 100 copies of your article, please contact author_reprints@wiley.co.uk
- To purchase reprints in smaller quantities, please visit http://www3.interscience.wiley.com/aboutus/ppv-articleselect.html. Restrictions apply to the use of reprints – if you have a specific query, please contact permissionsuk@wiley.com Corresponding authors are invited to inform their co-authors of the reprint options available
- To purchase a copy of the issue in which your article appears, please contact cs-journals@wiley.co.uk upon publication, quoting the article and volume/issue details
- Please note that regardless of the form in which they are acquired, reprints should not be resold, nor further disseminated in electronic or print form, nor deployed in part or in whole in any marketing, promotional or educational contexts without authorization from Wiley. Permissions requests should be directed to permissionsuk@wiley.com

Rock slope instability assessment using spatially distributed structural orientation data in Darjeeling Himalaya (India)

Saibal Ghosh,[1,3]* Andreas Günther,[2] Emmanuel John M. Carranza,[1] Cees J. van Westen[1] and Victor G. Jetten[1]

[1] Department of Earth System Analysis, International Institute for Geo-Information Science and Earth Observation (ITC), Enschede, The Netherlands
[2] Federal Institute for Geosciences and Natural Resources (BGR), Hanover, Germany
[3] Engineering Geology Division, Geological Survey of India, Eastern Region, Kolkata, India

*Correspondence to: Saibal Ghosh, ITC, Enschede, The Netherlands. E-mail: ghosh@itc.nl

ESPL

Earth Surface Processes and Landforms

ABSTRACT: We discuss a geographic information system (GIS)-based methodology for rock slope instability assessment based on geometrical relationships between topographic slopes and structural discontinuities in rocks. The methodology involves (a) regionalization of point observations of orientations (azimuth and dip) of structural discontinuities in rocks in order to generate a digital structural model (DStM), (b) testing the kinematical possibility of specific modes of rock slope failures by integrating DStMs and digital elevation model (DEM)-derived slope and aspect data and (c) computation of stability scenarios with respect to identified rock slope failure modes. We tested the methodology in an area of 90 km^2 in Darjeeling Himalaya (India) and in a small portion (9 km^2) within this area with higher density of field structural orientation data. The results of the study show better classification of rock slope instability in the smaller area with respect to known occurrences of deep-seated rockslides than with respect to shallow translational rockslides, implying that structural control is more important for deep-seated rockslides than for shallow translational rockslides. Results of scenario-based analysis show that, in rock slopes classified to be unstable, stress-induced rock slope instability tends to increase with increasing level of water saturation. The study demonstrates the usefulness of spatially distributed data of orientations structural discontinuities in rocks for medium- to small-scale classification of rock slope instability in mountainous terrains. Copyright © 2010 John Wiley & Sons, Ltd.

KEYWORDS: rock failure modes; digital structural model; discontinuity orientation; DEM; GIS; Darjeeling (India)

Introduction

In general, a slope becomes unstable when the shear stress acting on that slope exceeds the shear strength of the materials on that slope. One of the major factors governing the stability of rock slopes is directional anisotropy of planar structural discontinuities (e.g. foliations, joints and faults) in rocks (Romana, 1985; Selby, 1993; Orr, 1996; Hack *et al.*, 2003; Sitar *et al.*, 2005; Pantelidis, 2009). The presence of structural discontinuities in rocks contributes to both increase in shear stress acting on slopes and decrease of shear strength of slope materials. Discontinuity-controlled rock slope instability occurs in either natural or man-made ('engineered') rock slopes. This paper is concerned with spatial analysis of instability of natural rock slopes.

The geometrical relationships of structural discontinuities in rocks with topographic slopes define different modes of rock slope failures (plane, wedge or topple) (Goodman and Bray, 1976; Hoek and Bray, 1981; Matheson, 1983; Cruden, 1989; Roy and Mandal, 2009). The mode of discontinuity-controlled rock slope failure is also governed by the shearing strengths of structural discontinuities, which can be represented by their residual friction angles (Φ'_d). Data of Φ'_d may be derived through an empirical relationship with observed discontinuity-condition parameters available in the literature (Serafim and Pereira, 1983). Thus, spatially distributed data on orientations (azimuth, dip) of structural discontinuities in rocks and digital elevation model (DEM)-derived terrain properties (slope, aspect) are essential in kinematical testing of discontinuity-controlled rock slope failures and, thus, in scenario-based rock slope instability assessments.

The principles of different rock slope failure modes (plane, wedge or topple) are well-understood (Goodman and Bray, 1976; Hoek and Bray, 1981; Matheson, 1983; Cruden, 1989). Although applications of those principles to spatial analysis of rock slope instability at various mapping scales have been reported in the literature (e.g. Wagner *et al.*, 1988; Anbalagan, 1992; Carrara, 1999; Gupta *et al.*, 1999; Guzzetti *et al.*, 1999; Jaboyedoff *et al.*, 2004; Park *et al.*, 2005), very few attempts actually exist to incorporate spatially distributed data of structural discontinuity orientations in geographic information system (GIS)-based rock slope instability assessment

(Meentemeyer and Moody, 2000; Günther, 2003; Günther *et al.*, 2004). That is because modeling of the spatial distribution of structural discontinuity orientations is complex and is not commonly realized in a two-dimensional (2-D) GIS. Relative success has been achieved by using structural discontinuity orientation data in rock slope instability assessments at detailed to large scales (i.e. larger than 1 : 25 000) (Wagner *et al.*, 1988; Günther, 2003; Günther *et al.*, 2004; Günther and Thiel, 2009). However, using data of structural discontinuity orientations in rock slope instability assessment at medium to small scales (i.e. 1 : 25 000 or smaller) is even more challenging because such data are usually sparse due to, for example, poor rock exposures, thick vegetation and/or overburden cover, inaccessibility of the terrain, and high cost and/or non-availability of fine-resolution topographic data.

For application in rock slope instability assessment, point observations of three-dimensional (3-D) orientations of structural discontinuities in rocks must be regionalized (i.e. interpolated) into a continuous 2-D surface model of orientations of a certain type of geological structures. This surface model is referred to as a digital structural model (or DStM). In structurally complex terrains, the accuracy of a DStM depends on observation scale, data density, distribution and availability of suitable structural constraints such as trace-lines of major faults and fold axes. However, structural orientation data cannot be interpolated directly to create a DStM. For example, interpolation of azimuth data points of 330º and 30º can erroneously result in values about 150º (Meentemeyer and Moody, 2000; Günther, 2003). De Kemp (1998, 1999) proposed a concept for interpolation of structural orientation data by decomposing the unit vectors into three linear cosine components that can be used for 3-D interpolation. Günther (2003) followed this approach for 2-D constrained interpolation of each of the three cosine components and then integrating the results in order to derive DStMs for azimuths and for dips of a certain type of geological structure. Nevertheless, in complex structural terrains, irregularity and scarcity of spatially distributed structural orientation data as well as lack of structural constraints make DStM generation through conventional 2-D interpolation very problematic (Günther, 2003). In situations of data scarcity in large areas, deriving discrete directional information on individual rock discontinuity sets for suitable mapping units using vector statistical considerations (Wallbrecher, 1986; Swan and Sandilands, 1995) may be an alternative (Günther and Thiel, 2009).

In this paper, we discuss and apply suitable techniques for regionalization of point data of 3-D orientations of structural discontinuities in rocks in order to create DStMs at two different spatial scales. We utilize these DStMs together with DEM-derived terrain properties in order to (a) assess rock slope instability, (b) test the kinematical possibility of different modes of rock slope failures and (c) interpret their respective causal failure mechanisms. We then present a GIS-based technique of stress-induced rock slope instability analysis by incorporating different degrees of slope saturation. We first applied these techniques to a small area with a relatively high density and quite good distribution of structural data observation points, and then we applied the techniques to a larger area with relatively scarce and poor distribution of structural data observation points. We evaluated the results in both the test areas by quantifying the spatial association between the instability maps and the rockslide occurrence maps.

Study Area

The study area (90 km²) or Area B is comprised of the surroundings of Kurseong town (Darjeeling District, West Bengal, India) and is situated within the structurally complex and landslide-prone fold-thrust belt (FTB) in the Himalayas (Figures 1 and 2). Within the study area, a small test area (Area A in Figure 2) was selected in the north-western part of the study area. This test area (9 km²) was selected because it exhibits higher density and quite good distribution of structural orientation data and it has higher density of rockslides.

In the whole study area, topography is very rugged with elevations varying from 236 m to 2189 m and slopes varying from 0º to 84º. Climate in the area is humid with a long period (June–October) of monsoon-controlled heavy precipitation. Annual precipitation in the area varies from 2000 to 5000 mm
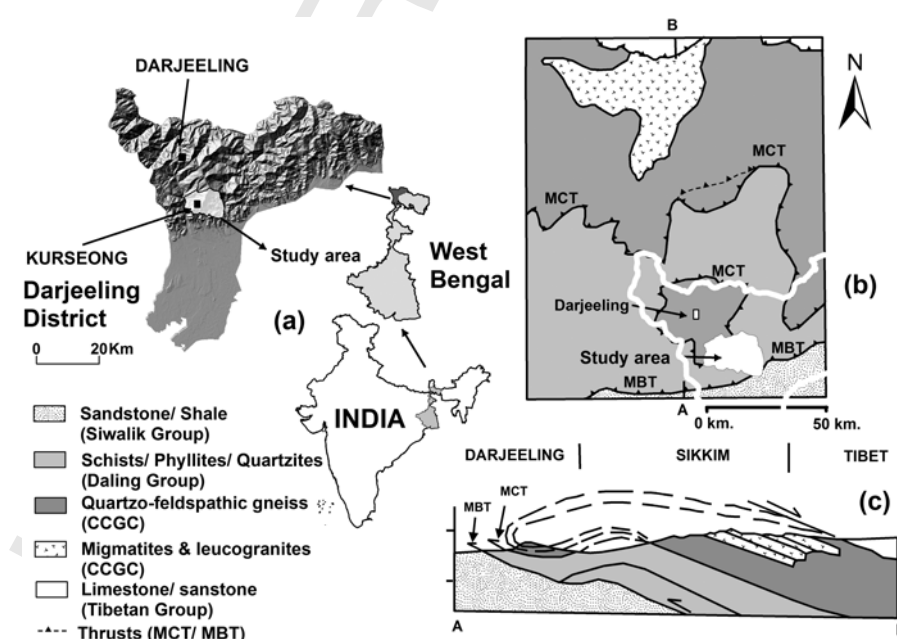

Figure 1. (a) Location of the study area. (b) Regional geological sketch map of Darjeeling-Sikkim Himalaya (adapted from Searle and Szule, 2005). (c) Schematic geological section of Darjeeling-Sikkim Himalaya (adapted from Searle and Szule, 2005).
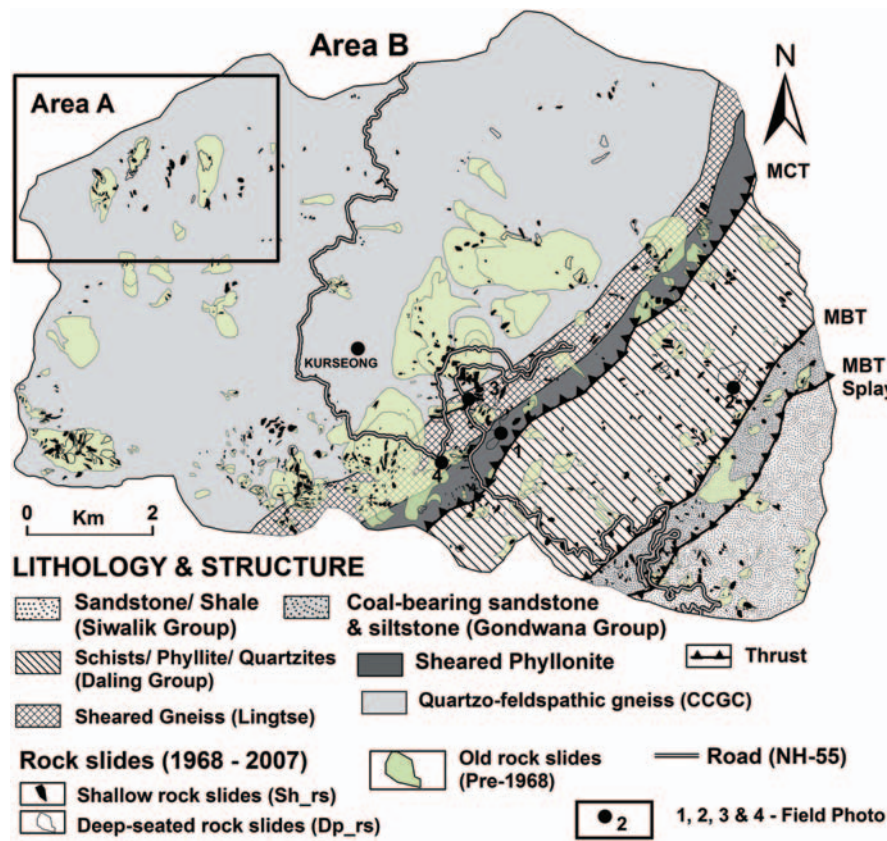
Figure 2. Geological map of the study area (Area B). Locations of recent (1968–2007) and areas of 'old and inactive' landslides are shown. Inset in the north-western part is the small test area (Area A).

(Soja and Starkel, 2007) with a very high precipitation density during the monsoon months, which makes the slopes become highly saturated and rainfall-triggered shallow landslides are common.

Geology and structural setting

The study area is part of a tectono-stratigraphic sequence of metamorphic rocks of the Himalayan FTB that borders the foreland molasse basin in the south (Figures 1b and 1c). The southern boundary of this Himalayan metamorphic sequence is marked by a high-strain ductile shear zone, called the main central thrust (MCT), coinciding with an inverted sequence of metamorphic rocks from kyanite grade to biotite-chlorite grade (Hubbard, 1996; Searle and Szule, 2005) of the central crystalline gneissic complex (CCGC). Tectono-stratigraphically, the terrain where the study area is situated represents the southern part of the Darjeeling klippe (Figure 1b), where high grade metamorphic rocks of the CCGC are thrusted over the low grade meta-sedimentary rocks (schists/phyllites and quartzites) of the Daling Group along the MCT (Mallet, 1875; Sinha-Roy, 1982). Further to the south, the foreland molasse sediments (sandstone/shale) of the Siwalik Group are underlain by a thin intra-thrusted slice of minor coal-bearing clastic rocks (sandstone/siltstone) of the Gondwana Group. Towards the north, these Gondwana rocks are thrusted over by the Daling Group of meta-sediments along the southern-most front of Himalayan FTB known as the main boundary thrust (MBT). The MCT and MBT represent the main regional structural features in the studied terrain (Figures 1 and 2). Along the basal part of MCT, a sheared phyllonite is exposed, and towards its immediate north, a thin intra-thrusted slice of

coarse-grained sheared gneissic rocks (Lingtse Gneiss) is present as a prominent marker lithology adjacent to MCT in this part of eastern Himalayan FTB (Figure 2).

The CCGC, the Daling meta-sediments and other associated rocks in the FTB are overturned (towards north) and highly foliated, with foliations generally dipping towards north to northwest with moderate inclinations ranging from 30º to 50º. Due to intense (ductile and brittle) deformation, the rocks in the FTB are folded, faulted and thrusted. Therefore, local variations in dip and dip direction of bedding and foliation planes are quite prominent. The mapped thrusts and some faults (Figure 2) were confirmed from discrete field observations of the presence of mylonitic fabric near ductile thrust zones, sudden steepening of beds, rotation of foliation surfaces and slickensides. Due to associated brittle deformation, the rocks in the FTB are also highly fractured and jointed.

Rockslides and slope failure modes – their relation with geomorphology, structure and meteorological trigger

In the Darjeeling Himalaya, active erosion occurs on moderate to steep slopes, resulting in continuous supply of large amounts of colluvial materials along depressions and flat depositional sites towards the south. On a catchment scale, these denudation processes are controlled mostly by southerly-flowing streams that are transverse to the main east-northeast (ENE) trend of Himalayan thrust planes (Figure 2). Slopes are gentler on ridge tops but become increasingly steeper downward to the stream banks. The stream pattern generally follows structurally weak planes, which facilitate
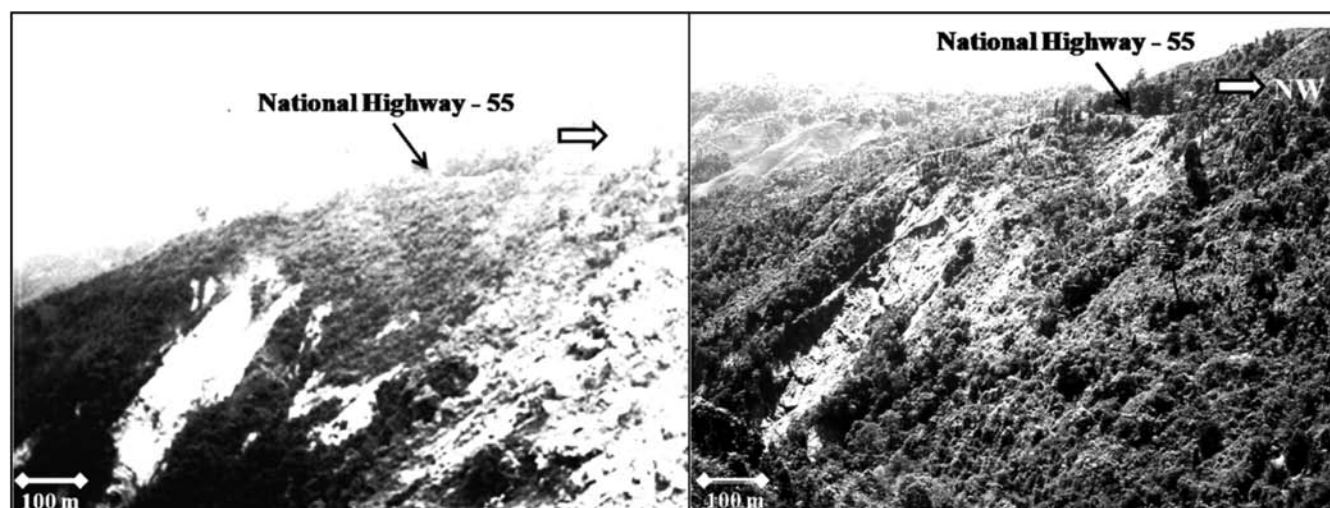
Figure 3. Retrogression of a deep-seated rock wedge slide (see 1 in Figure 2). Photograph on the left (taken in 2001) shows the failure initiation in the lower portion of the steep slope possibly due to under-cutting along the stream just above the toe of the slide. Photograph on the right (taken in 2008) shows that the same slide has retrogressed upwards to the elevation of National Highway-55.

entrenchment of streams (Dutta, 1966). The steepening of the valley slopes is attributed to the rapid rate of under-cutting and/or toe-erosion by the streams, which are inherently associated with active tectonic uplift (c. 6·9 ± 1·8 mm/yr) of the Himalayan FTB (Burbank et al., 1996; Wesnousky et al., 1999). Consequently, rock slope failures generally initiate on slopes that are proximal to the streams, facilitating daylighting of bedrock discontinuities and subsequently resulting in a series of large deep-seated retrogressive rock slope failures in the course of time (Figures 2 and 3). On the contrary, smaller shallow translational rockslides occur in weathered, highly-fractured and steep slopes depending on geometric relationships between structural discontinuities and topography. Some shallow translational rockslides occur near road cuts, where natural rock slopes artificially steepen at local scales. Occasionally along road-cuts, bad drainage systems are instrumental in causing differential saturation, which easily trigger shallow landslides. Shallow landslides generally require less amount of triggering rainfall, whereas deep-seated land-slides generally require longer periods of triggering rainfall (cf. Aleotti, 2004; Dapporto et al., 2005).

In the study area, plane, topple and wedge modes of rock slope failures are commonly observed in either shallow or deep-seated rockslides (Figure 4), although wedge failures are more predominant (Figure 4a). There is high possibility of occurrence of all three modes of rock slope failure in the study area because of the varying topographic and structural geo-logical conditions as well as the varied joint shear strengths, which justify spatially distributed deterministic assessment of rock slope instability.

In addition to active shallow and deep-seated rockslides, we have outlined several areas of large 'old and inactive' slides (cf. UNESCO-WP/WLI, 1993) in the study area (Figure 2). We call these areas 'old and inactive' slides because their characteristics in 1980 aerial photographs clearly suggest evidence of landsliding (e.g. presence of scarps) although they are covered by vegetation and there are no historic records or legacy maps indicating those areas to be landslides. However, our landslide inventory (Ghosh et al., 2009) shows that about 70% of the areas of mapped landslides that occurred within the period of 1968 to 2007 are located within the scarps of those 'old and inactive' slide areas (Figure 2). This suggests that rock slope failure mechanisms similar to those of the 1968–2007 rockslides were operative prior to 1968. For the purpose of evaluating our rock slope instability assessment, we preferred to use the mapped rockslides that occurred within the period 1968–2007.

Datasets

During fieldwork, we were able to measure dip (azimuth normal) directions and dip values of 315 foliation/bedding (Fol) planes and 514 joint surfaces at 315 accessible locations (Figure 5). Via cluster analysis, we divided the joint orientation data into four sets, namely J1 (southwesterly-dipping), J2 (southeasterly-dipping), J3 (northwesterly-dipping) and J4 (northeasterly-dipping). Thus, we have five sets of data of structural discontinuity orientations. In order to visualize the variability in structural discontinuity orientations, we plotted the poles-to-planes of each of the five structural orientation data sets in a synoptic fabric diagram (Figure 6), which indicates respective mean vector discontinuity orientation in each data set together with the respective vector statistical parameters such as confidence cone, spherical aperture and eigen-vectors (cf. Wallbrecher, 1986). Each of the structural discontinuity orientation data set shows a high degree of conformity of measurements (75–87%), very small confidential cones (3°–4°), and reasonable spherical apertures (21°–30°). The azimuth/dip orientation of mean vectors of Fol, J1, J2, J3 and J4 data sets are 328°/24°, 227°/68°, 140°/68°, 312°/67° and 053°/65°, respectively (Table I, Figure 6).

At some of the 315 accessible locations, we were able to confirm the presence of major thrusts and faults that we have compiled from old geological maps (Mallet, 1875; Acharya and Ray, 1977) and some of the linear structural features we have interpreted in stereo-pairs of 1:10 000 scale aerial photographs (Figure 5). We then used the map of confirmed map traces of major thrusts/faults/fractures as primary structural constraints for generating DStMs of structural orientation data for each set of structural discontinuities (see section on 'Spatial modeling of structural discontinuity orientations').

Following the guidelines of Bieniawski (1989) for rock mass rating (RMR) classification, we were able to obtain data at 240 of the 315 accessible locations for joint condition parameters (i.e. spacing, length/persistence, infilling, roughness, separation and weathering condition). In general, the observed joints have average spacing of <40 cm, persistency of up to 1–3 m or more
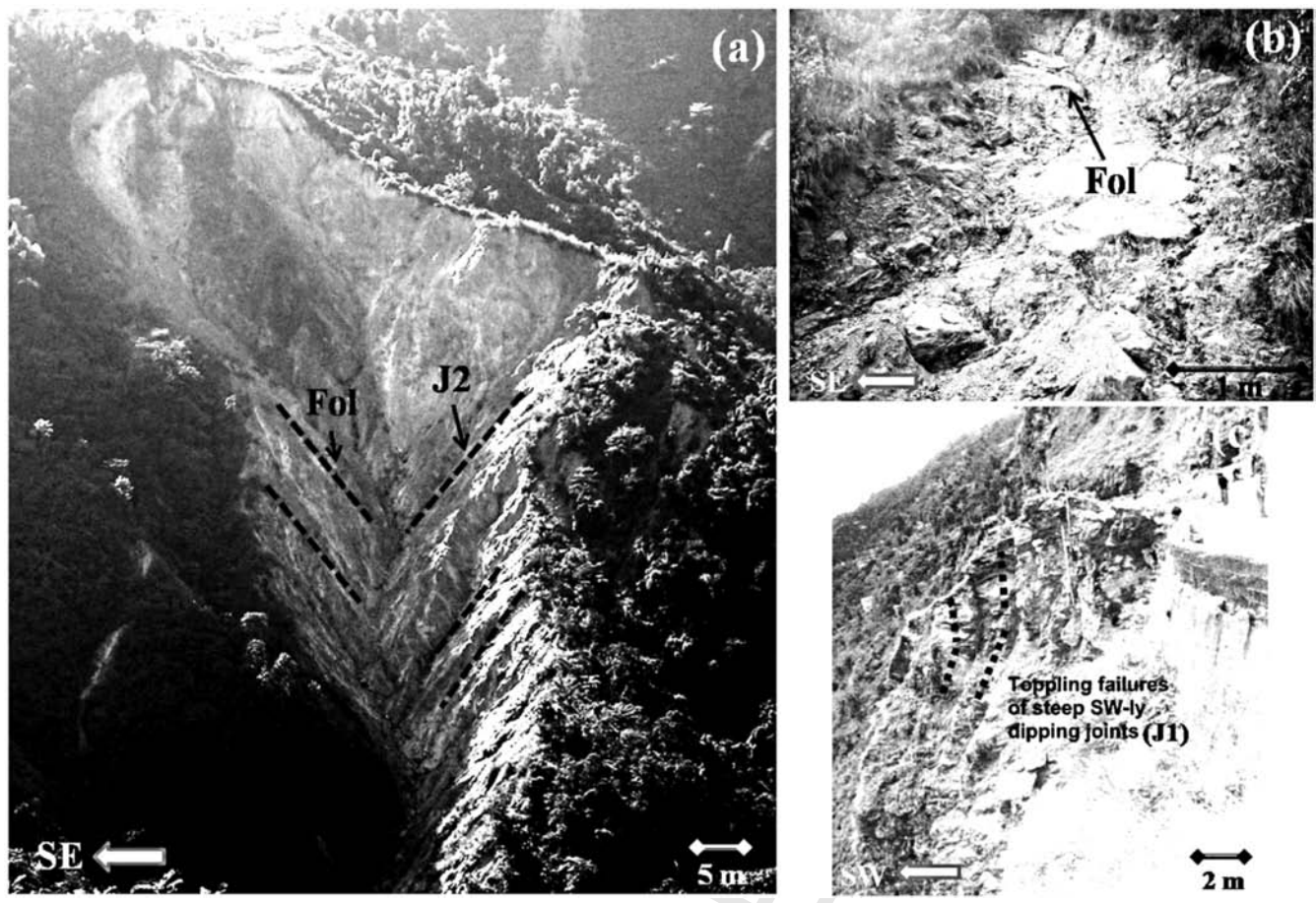
Figure 4. Different modes of rock slope failures in the study area. (a) A deep-seated rock wedge (W_Fol_J2) within Daling metasediments (see 2 in Figure 2). (b) Plane failure (P_Fol) along foliation surface (Fol) in sheared phyllonitic rocks (see 3 in Figure 2). (c) Toppling (T_J1) caused by steeply-dipping southwest(SW)-dipping joints (J1) within quartzo-feldspathic gneiss (see 4 in Figure 2).

and are smooth to rough planar. The walls of the observed joints vary from un-weathered and weathered and generally do not exhibit perceptible separation. Minor infilling (<1 mm) of crushed silty materials are present in slightly open joint walls. Among the four joint sets (J1, J2, J3 and J4), no significant variations in conditional properties were observed.

Using the measured joint condition parameters, we derived values of Φ'_d at each of the 240 locations based on the empirical relation of Serafim and Pereira (1983). The empirically-derived values of Φ'_d vary between 22° and 36°. After performing spatial autocorrelation analysis on the empirically-derived values of Φ'_d, we applied inverse-distance weighting (IDW) interpolation with a power of two and a minimum of 15 data points within a search radius of 5 km. We followed a jack-knife (or omit one data point) approach in order to derive the best-fit surface model of Φ'_d (i.e. we performed interpolation 240 times, each time with 239 data points and each surface model was cross-validated with the respective single data point omitted in the analysis). Our best surface model of empirically-derived values of Φ'_d (Figure 7) has a root mean square error of four for interpolation data points and a squared difference of zero for the respective cross-validation data point. We used this surface model of empirically-derived values of Φ'_d (Figure 7) as a spatially distributed shearing strength parameter of discontinuity, instead of using a single arbitrary global value of Φ'_d as proposed by Aksoy and Ercanoglu (2007), in testing the kinematical possibility of specific modes of rock slope failures in the test areas (see section on 'Kinematical testing of rock slope instability').

For topographic data, we used a 10 m × 10 m pixel resolution 'CartoDEM' that was prepared through photogrammetric techniques (in the LPS suite of ERDAS Imagine 9·2) using stereo-images of 2·5 m resolution IRS P5 Cartosat-1 satellite data of 2006. In order to generate a high-precision CartoDEM, we ortho-rectified the stereo Cartosat images by using 16 ground control points (GCPs) measured through differential global positioning systems (GPS) in the field. For geo-referencing, we used WGS 84 as datum and projected the scenes in UTM (Zone 45N). From the CartoDEM, we used ArcGIS 9·3 to derive raster maps of slope and aspect, which were used as topographic inputs for both areas. In addition, we prepared another 10 m × 10 m pixel resolution 'TopoDEM' by interpolation of 10 m interval contour lines that were digitized from a 1 : 25 000 scale topographic map of 1969. Despite of its poor resolution compared to that of the CartoDEM, we used the TopoDEM because it is the only available topographic data available for examining rock slope instability conditions in the study area for the period prior to our 1968–2007 rockslide inventory (see section on 'Kinematical testing of rock slope instability').

In addition to the primary and secondary structural data and the DEMs and DEM-derived slope and aspect maps, we compiled and/or mapped outlines of landslides from different temporal data sources, which include a 1 : 25 000 scale topographic map of 1969, 1 : 10 000 scale aerial photographs of 1980, ground-surveyed landslide maps of 1993, 1998 and 2007, Indian Remote Sensing Satellite images like IRS-1D PAN (5·8 m resolution) of 2002, IRS P6 LISS 4 MX (5·8 m resolution) of 2004, and stereo IRS P5 Cartosat images (2·5 m resolu-
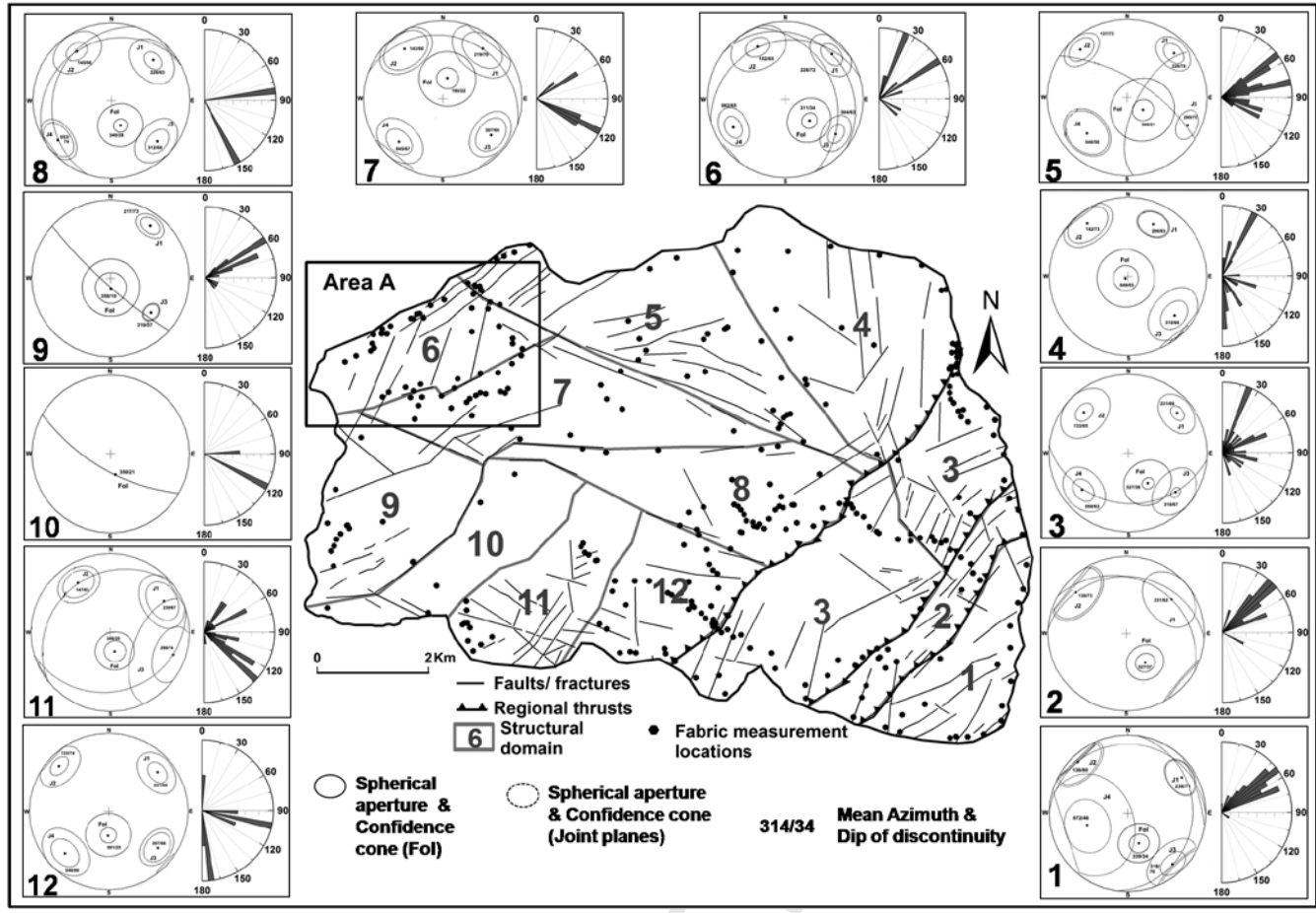
Figure 5. Map of Area B showing locations of fabric (orientation) measurements, mapped thrusts/faults/fractures and boundaries of 12 interpreted structural domains. Also shown for individual domains are equal-area projection nets and uni-directional rose plots (5°-intervals of strike directions) of faults/fractures. For each domain, see Table IV for vector statistics (mean orientation, spherical aperture and confidence cone) of measured fabric orientations of each discontinuity set and see Table III for strikes of the mapped faults/fractures.

Table I. Vector statistics of measured discontinuity orientations (in the entire study area – Area B)

Discontinuity set	Data (number)	Mean orientation (azimuth/dip)	Confidential cone	Spherical aperture	Eigenvectors (azimuth/dip)			Degree of conformity	K value of Woodcock (1977)
					E1	E2	E3		
Fol	315	328°/24°	3°	30°	245°/03°	337°/26°	149°/63°	74·52%	0·27
J1	166	227°/68°	3°	22°	211°/67°	315°/06°	047°/22°	86·06%	0·56
J2	158	140°/68°	4°	25°	155°/68°	052°/05°	320°/22°	82·52%	0·79
J3	92	312°/67°	4°	21°	309°/67°	041°/01°	132°/23°	86·8%	0·84
J4	98	053°/65°	4°	24°	051°/65°	143°/01°	233°/25°	83·57%	0·56

tion) of 2006 (Ghosh *et al.*, 2009). Based on ground-truthing of compiled/mapped landslides and on the landslide classification proposed by Varnes (1978), we prepared a comprehensive multi-temporal inventory and spatial database of landslides. Among the different types of landslides in the area, we distinguish between shallow translational rockslides (hereafter denoted as Sh_rs) and deep-seated rocks slides (hereafter denoted as Dp_rs) by using a threshold depth to failure surface of 5 m. We used maps of Sh_rs and Dp_rs (Figure 2) to evaluate the results of our rock slope instability assessment (see section on 'Evaluation of rock slope instability maps').

Spatial Modeling of Structural Discontinuity Orientations

Considering the differences in density and distribution of structural discontinuity orientation data and the differences in

amount of structural constraints in test Areas A and B (Figure 5), we apply different regionalization techniques in order to create DStMs for the two test areas. In Area A, where point data of structural discontinuity orientations are quite dense and well-distributed, regionalization of such data involves interpolation. In Area B (i.e. the whole study area), where point data of structural discontinuity orientations are quite sparse and poorly-distributed, regionalization of such data involves generalization.

DStM generation in Area A

For Area A, we follow the technique proposed by Günther (2003) to interpolate 3-D orientation or fabric measurements for individual types (or sets) of structural discontinues in rocks at every observation point. The interpolation process (Günther, 2003) involves (a) decomposition of orientation data (i.e. unit

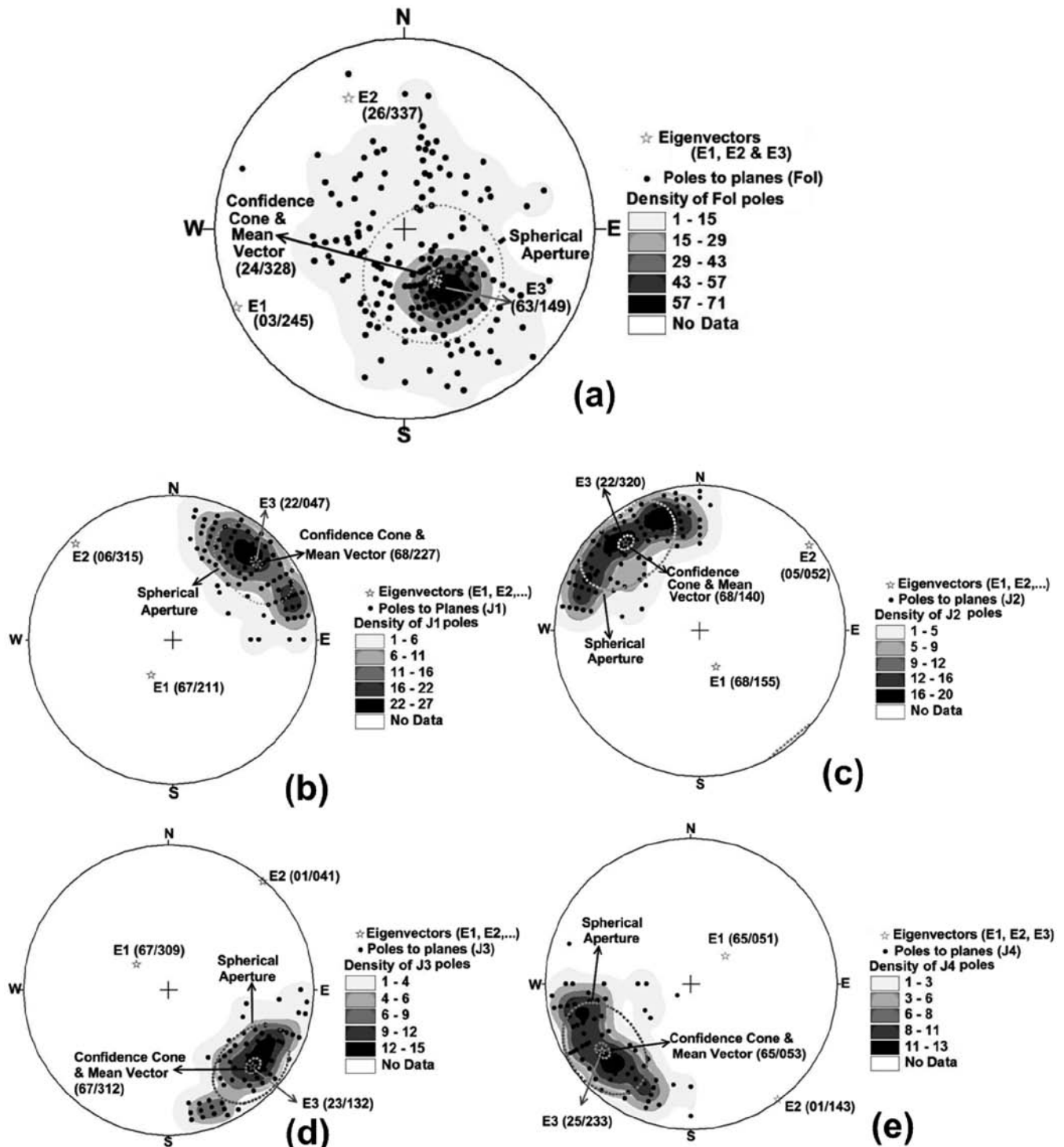Copyright © 2010 John Wiley & Sons, Ltd.

Earth Surf. Process. Landforms, Vol. **35**, 000–000 (2010)

Figure 6. Synoptic fabric plots of poles to five measured discontinuity planes in an equal area projection (Schmidt's projection, lower hemisphere) along with the plot of mean vectors, confidential cones and spherical apertures and eigenvectors for (a) foliation plane (Fol), (b) joint set J1, (c) joint set J2, (d) joint set J3 and (e) joint set J4.

vectors having only directions) into three linear cosine components [cos(α), cos(β) and cos(χ); see De Kemp (1998) for details] followed by separate interpolation of each cosine component and (b) conversion of the interpolated linear cosine components into rasters (i.e. DStMs) of azimuth and dip. Mapped structural constraints (major faults/thrusts) are incorporated as barriers (i.e. linear features known to interrupt the resulting surface geometry) into the interpolation process. We applied IDW interpolation because it does not produce pixel values out of the input data range, which is important

for the interpolation of unit vector components since values of either cos(α) or cos(β) must be in the [−1,+1] range and values of cos(χ) must be in the [0,1] range. We used a power of two in IDW interpolation so as to give stronger weights to pixels of and close to the original input data than pixels farther away. As in the IDW interpolation of values, we followed a jack-knife approach to derive best-fit DStMs of azimuth and dip of each set of structural discontinuities in rocks.

Figure 8 shows the DStMs for azimuth and dip of Fol, whereas Table II shows the vector statistics of measured ori-
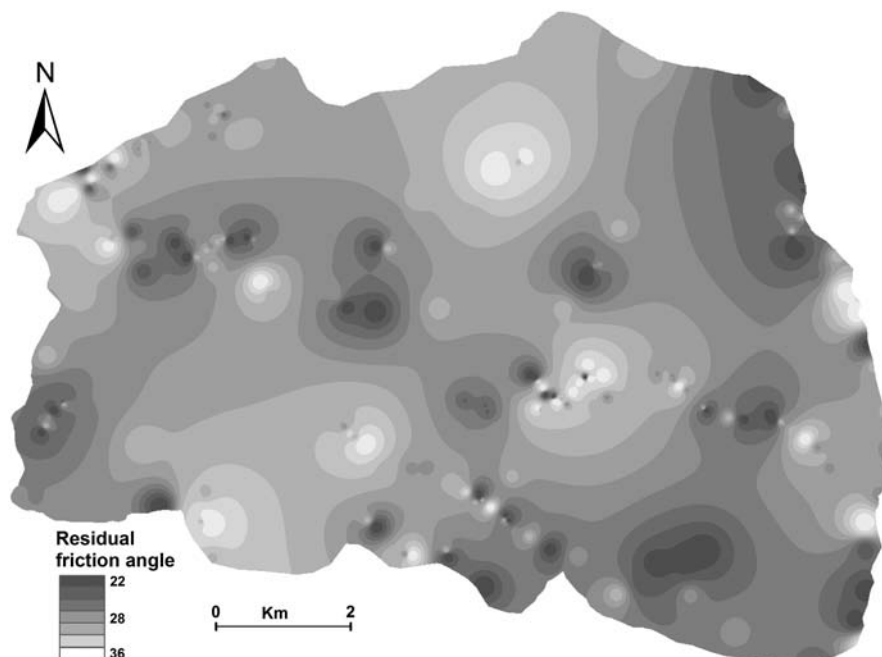
Figure 7. Map of interpolated residual friction angles of structural discontinuities.
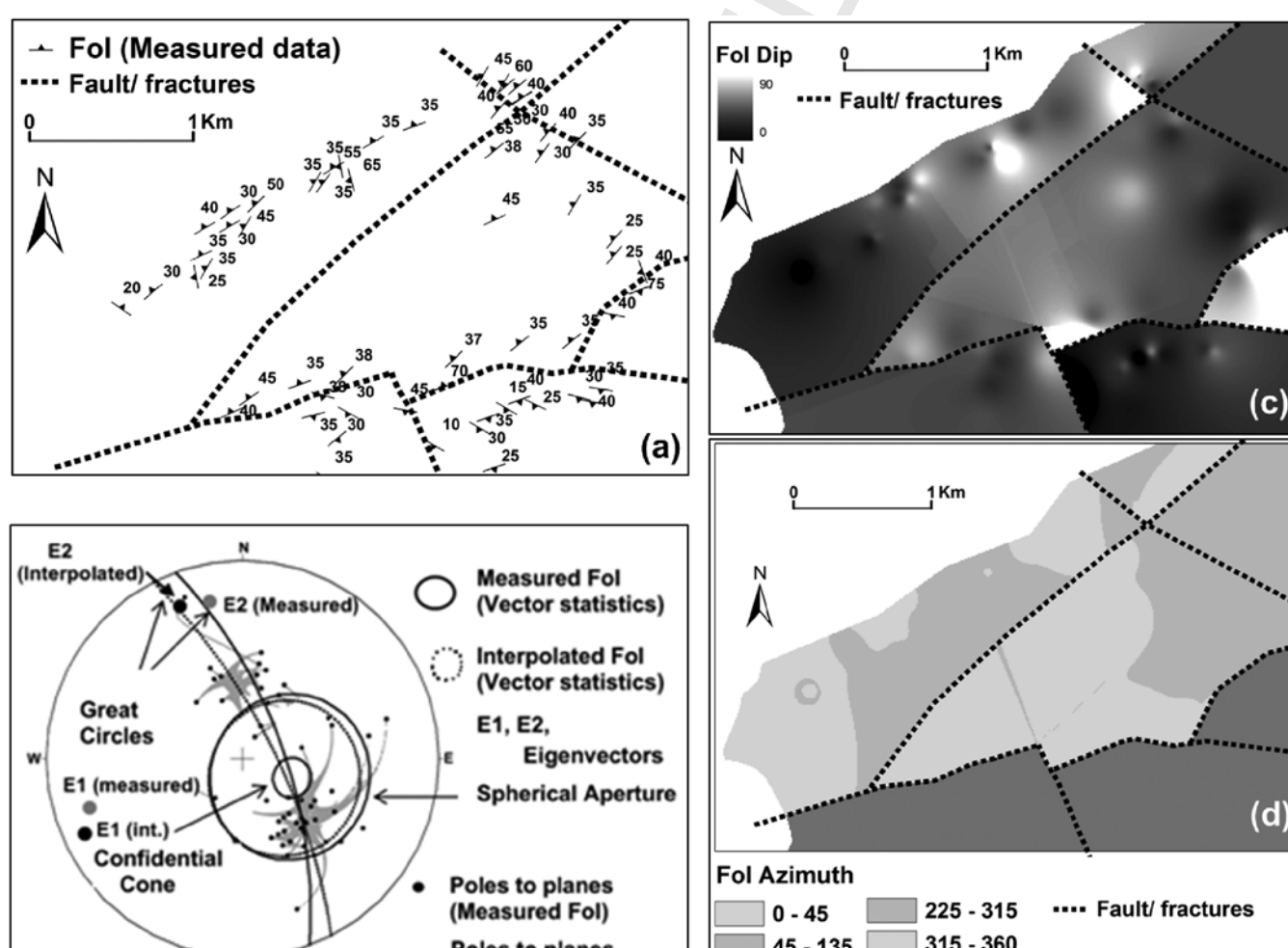
Figure 8. Distribution of orientation data for foliation (Fol), their respective DStMs and equal area projection nets of measured data and interpolated values of Fol in Area A. (a) Locations of measured orientation data for foliation (Fol). (b) Plot of 'poles-to-plane' (showing spherical apertures, confidence cones, eigenvectors and great circles) of measured Fol orientations and their respective interpolated orientations in DStMs. (c) DStM of Fol dip. (d) DStM of Fol azimuth. See Table II for vector statistics of measured and interpolated orientation data.

Table II. Vector statistics of measured discontinuity orientations and interpolated discontinuity orientations in DStMs

Discontinuity set	Data (number)	Mean orientation (azimuth/dip)	Confidential cone	Spherical aperture	Eigenvectors (azimuth/dip)			Great circle alignment	Small circle alignment
					E1	E2	E3		
Fol (Measured)	63	291°/22°	8°	34°	250°/17°	346°/18°	120°/64°	54%	–
Fol (Interpolated)	90349	295°/20°	0°	32°	243°/13°	338°/22°	125°/64°	77%	–
J1 (Measured)	30	225°/71°	7°	22°	207°/70°	313°/05°	045°/19°	47%	17%
J1 (Interpolated)	86618	220°/67°	0°	14°	257°/62°	136°/15°	040°/23°	14%	50%
J2 (Measured)	35	146°/66°	8°	27°	158°/66°	058°/04°	326°/24°	42%	27%
J2 (Interpolated)	86620	148°/67°	0°	14°	181°/63°	064°/13°	328°/23°	14%	50%
J3 (Measured)	14	313°/66°	11°	22°	328°/65°	226°/06°	133°/25°	32%	30%
J3 (Interpolated)	89836	311°/68°	0°	16°	266°/60°	033°/19°	131°/22°	19%	40%
J4 (Measured)	28	057°/65°	8°	23°	054°/65°	147°/01°	238°/25°	44%	18%
J4 (Interpolated	75187	058°/66°	0°	13°	061°/66°	329°/01°	238°/24°	26%	25%

Table III. Attributes of photo-interpreted lineaments (faults/fractures) in individual structural domains (Figure 5)

Domain	Number of lineaments	Strike maxima of lineaments	Lineament density (mean)	Principal basis for delineation of domain boundary
1	22	055°	2·74	Thrust boundary, lineament density
2	24	045°	3·78	Thrust boundary, lineament density
3	40	023°	2·28	Thrust boundary, strike maxima of lineaments, lineament density
4	19	024°	1·47	Strike maxima of lineaments, lineament density
5	21	055° and 080°	1·99	Strike maxima of lineaments, lineament density
6	18	023° and 055°	2·20	Strike maxima of lineaments, lineament density
7	22	115°	1·51	Strike maxima of lineaments, lineament density
8	11	085° and 155°	0·99	Fracture density
9	19	057°	1·54	Strike maxima of lineaments, lineament density
10	9	120°	0·85	Strike maxima of lineaments, lineament density
11	29	135°	2·31	Strike maxima of lineaments, lineament density
12	12	100° and 170°	1·48	Thrust boundary, strike maxima of lineaments, lineament density

entation data and the interpolated values in DStMs. The averages of interpolated Fol orientations are closely similar to the averages of measured Fol orientations (Table II). Both poles-to-planes projections of measured and interpolated Fol orientations are aligned to steep great circles with π-poles of 250°/17° and 243°/13°, respectively (Figure 8b). The fabric shape of the original Fol data is closely resembled by the DStMs of Fol, as indicated by their nearly identical spherical apertures, great circle alignments and near-similar eigenvector orientations and magnitudes (Figure 8, Table II). In the raster maps of interpolated Fol orientations (Figures 8c and 8d), abrupt changes of Fol orientations at the breaklines seem to be artifacts but they actually represent near-real ground situations. In the interpolation process the breaklines act as interpolation 'barriers' so that fabric orientations are offset along the thrusts/faults (e.g. the nearly east-west (E-W) trending fault passing through a valley in Figure 8), which we also observed during fieldwork.

The same technique was applied to the orientation data of each of the four joint sets, J1 to J4. For each of the joint sets, the means of interpolated values in the DStMs are much more closely similar to the means of the measured data, as indicated by the smaller spherical apertures and fabric shape eccentricities derived from the eigenvectors (Table II). In general, a good fit of vectorial orientation between the measured data and the interpolated values is observed for all the five structural discontinuity sets.

DStM generation in Area B

We subdivided the whole study area into 12 structural domains in terms of presence of major thrusts/faults as natural structural

boundaries, predominant strike (or azimuth) of faults/fractures and fracture density (Figure 5). Where traces of the major thrusts/faults were not confirmed by our fieldwork, we demarcated the structural domains based on changes in the dominant strike maxima of mapped fault/fracture systems and on differences in fracture densities (Figure 5, Table III). Spatial distribution of fracture density is modeled via interpolation of density of mapped fracture/fault/thrust traces considering 500 m as search radius. The purpose of subdividing the whole study area into structural domains was to create smaller areas of influence for regionalization of structural orientation data. Subsequently, in each structural domain, structural discontinuity orientations were regionalized by computing and using the mean integer values of measured orientations of each set of structural discontinuities (Fol, J1, J2, J3 and J4) (Figure 5, Table IV) in order to create two raster grids (one for azimuth, one for dip).

Kinematical testing of rock slope instability

Identification of modes of rock slope failure

By using the raster maps of DStMs, Φ'_d values, slopes and aspects, the kinematical possibility of a certain mode of discontinuity-controlled rock slope failure (plane, wedge and topple) can be tested for every pixel in the map (Günther, 2003). Plane failure is kinematically possible if the dip of a controlling structural discontinuity is steeper than the residual friction angle of discontinuity (Φ'_d) and shallower than the apparent inclination of the slope with aspect the same as or similar to the dip direction of the structural discontinuity (Figure 9a). Wedge failure is kinematically possible if the above condition for plane failure is met by the cutting line or

Table IV. Vector statistics and mean values of azimuth and dip data of foliations (Fol) and joint sets (J1 to J4) per structural domain (Figure 5, Table III)

Structure set	Vector statistics	Structural domains											
		1	2	3	4	5	6	7	8	9	10	11	12
Fol	Data (number)	18	16	57	23	33	33	26	38	16	5	16	34
	Spherical aperture (deg)	21	19	24	30	33	23	29	23	30	–	20	23
	Confidential cone (deg)	10	10	6	13	11	8	11	7	16	–	11	8
	Conformity (%)	87	89	84	74	71	84	77	84	75	69	88	84
	Mean azimuth/dip (deg)	339/34	327/37	327/38	049/03	309/21	311/34	193/22	340/28	233/16	350/21	346/20	001/25
J1	Data (number)	8	5	28	8	15	16	12	24	11	1	11	17
	Spherical aperture (deg)	16	28	19	14	17	21	28	23	13	–	25	20
	Confidential cone (deg)	17	0	7	15	10	11	19	9	9	–	18	10
	Conformity (%)	93	78	89	94	92	87	79	85	95	–	82	88
	Mean azimuth/dip (deg)	236/71	231/62	231/69	206/63	226/70	226/72	219/70	226/63	217/73	205/75	239/67	231/68
J2	Data (number)	8	8	27	10	12	24	10	24	3	1	11	19
	Spherical aperture (deg)	21	25	25	23	17	26	25	23	–	–	20	20
	Confidential cone (deg)	23	27	9	19	12	11	21	10	–	–	15	9
	Conformity (%)	87	82	83	84	91	80	82	84	–	–	88	89
	Mean azimuth/dip (deg)	136/80	130/73	133/65	142/73	137/73	152/65	143/68	145/66	122/73	175/75	147/63	133/74
J3	Data (number)	6	2	5	6	5	6	11	15	9	–	6	11
	Spherical aperture (deg)	12	–	5	14	13	9	22	22	9	–	24	18
	Confidential cone (deg)	24	–	23	26	62	17	16	12	8	–	47	14
	Conformity (%)	95	–	99	94	95	97	87	86	98	–	83	90
	Mean azimuth/dip (deg)	318/76	334/67	310/67	310/66	295/72	304/68	307/66	312/68	310/57	–	290/74	307/66
J4	Data (number)	6	4	18	4	8	16	15	10	4	–	1	14
	Spherical aperture (deg)	26	–	22	–	22	18	23	19	–	–	–	24
	Confidential cone (deg)	51	–	11	–	24	10	13	16	–	–	–	14
	Conformity (%)	81	–	86	–	86	90	85	89	–	–	–	84
	Mean azimuth/dip (deg)	072/46	053/68	050/63	045/61	048/58	062/65	045/67	053/74	065/50	–	–	046/66

Copyright © 2010 John Wiley & Sons, Ltd.

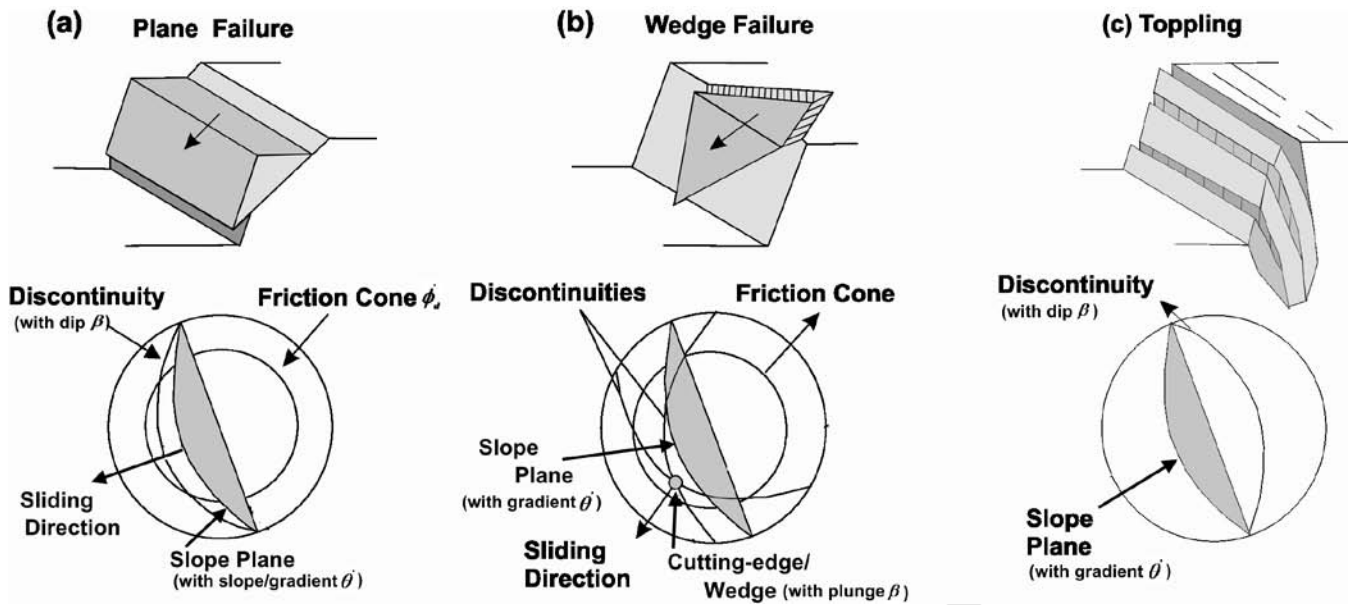Earth Surf. Process. Landforms, Vol. **35**, 000–000 (2010)

Figure 9. Modes of different rock slope failures (after Goodman and Bray, 1976; Hoek and Bray, 1981).

wedge axis between two structural discontinuity surfaces (Figure 9b). Plane topple is kinematically possible if a nearly vertical structural discontinuity strikes sub-parallel to a nearly vertical slope with aspect the same as or similar to the dip direction of the structural discontinuity (Figure 9c). Wedge topple is kinematically possible if nearly vertical cutting lines or wedge axes between two structural discontinuity surfaces strike sub-parallel to a nearly vertical slope with aspect the same as or similar to the plunge direction of the cutting lines or wedge axes (cf. Jaboyedoff et al., 2009). For any failure mode, the controlling structural discontinuity or cutting line(s) may either dip/plunge into the slope with $\beta \leq 90°$ (Goodman and Bray, 1976) or out of the slope with $\beta > 90°$ (Cruden, 1989), where β is the inclination of the discontinuity or cutting line measured from the dip direction of the slope normal.

Based on raster maps of raster maps of DStMs, Φ'_d values, slopes and aspects, the foregoing criteria for kinematical possibility of certain modes of rock slope failure are evaluated in the SlopeMap module of the RSS-GIS software by applying the following conditions at every pixel in the maps:

$$\Phi'_d \leq \beta \leq \theta' \text{ (for plane and wedge sliding); and} \quad (1)$$

$$\theta' \geq [\Phi'_d + (90° - \beta)] \text{(for plane and wedge topple),} \quad (2)$$

where θ' is the apparent dip/inclination of the topography with aspect the same as or similar to the dip direction of the controlling structural discontinuity or the plunge direction of the controlling cutting line(s).

If any of the above relations is true for a pixel, SlopeMap returns a value of one for that pixel meaning that a particular failure mode is kinematically possible; otherwise, SlopeMap returns a 'null' value for that pixel meaning that a particular failure mode is kinematically impossible (Günther, 2003). The returned values for every pixel where one or more failure modes in kinematically possibly can then be combined so that rock slope instability according to one or more failure mode can be assessed for every pixel.

Rock slope instability in Area A

The DStMs for each of the five sets of structural discontinuities and their 10 mutual cutting lines, the raster map of Φ'_d values,

and raster maps of slope and aspect derived from the 10-m resolution CartoDEM of 2006 were used to identify 10 m × 10 m pixels where certain modes of rock slope failures are kinematically possible. Theoretically, the five sets of structural discontinuities and their 10 cutting lines can result in 30 possible failure mechanisms, meaning failure modes due to one or more set of structural discontinuities. In Area A, the analysis resulted in 22 out of the 30 possible failure mechanisms (Table V). For example, out of five possible plane failure mechanisms, P_J2 (read as plane failure due to joint set J2) is almost impossible except in one pixel (Table V, Figure 10). Therefore, joint set J2 does not contribute significantly to rock slope instability in Area A.

The results given in Table V and shown in Figures 10(a)–10(c) can be summarized as follows. For possibility of plane failure mode, bedding plane/foliation (P_Fol) provides the highest contribution of 74% to rock slope instability, followed by joint set J3 (P_J3) with 22% contribution. Of the 10 possible failure mechanisms that could cause wedge rock failures, prominent contributions to rock slope instability are provided by failure mechanisms W_J1_J4 (40%), W_J2_J3 (29%) and W_Fol_J1 (19%). Only eight of the 15 possible topple mechanisms (both plane and wedge topples) could possibly result in topple failures, and prominent contributions to rock slope instability are provided by topple mechanisms T_J2 (45%) and T_J3 (34%). Wedge topple mechanisms are comparatively less possible than the plane topples, because among the 10 possible wedge topple mechanisms, only four wedge topples involving the four joint sets are kinematically possible. Mostly cutting-lines between joints with steep plunges (i.e. > 70°) generally contribute to the wedge topples, which are relatively a rare possibility in the study area.

Because multiple discontinuity-controlled failure mechanisms are possible in any portion of the terrain, determining pixels where one or more failure modes are possible (i.e. failure mode count) is an intuitive measure of rock slope instability. Therefore, we extended our analysis by presenting a map of failure mode count for every pixel in order to identify pixels where multiple failure modes and multiple failure mechanisms are kinematically possible (Figure 10d, Table V). The result shown in Figure 10(d) suggests that there is possibility for any mode of rock slope failure in 17% of Area A ($1·5$ km^2), in 70% of which there is possibility for at least one failure mode and in 30% of which there is possibility for

Table V. Number of pixels where different discontinuity-controlled failure modes and their respective failure mechanisms are kinematically possible in Area A

Failure mode	Failure mechanisms	Number of pixels
Plane	P_fol	1098
	P_J1	35
	P_J2	0
	P_J3	327
	P_J4	19
	Planar_all	1479
	With 1 failure	1479
	With >1 failure	0
Wedge	W_Fol_J1	2006
	W_Fol_J2	315
	W_Fol_J3	348
	W_Fol_J4	483
	W_J1_J2	67
	W_J1_J3	90
	W_J1_J4	4173
	W_J2_J3	2979
	W_J2_j4	249
	W_J3_J4	695
	Wedge_all	10340
	With 1 failure	9327
	With >1 failure	1013
Topple	T_Fol	0
	T_J1	1079
	T_J2	3130
	T_J3	2333
	T_J4	774
	T_Fol_J1	0
	T_Fol_J2	0
	T_Fol_J3	0
	T_Fol_J4	0
	T_J1_J2	618
	T_J1_J3	18
	T_J1_J4	0
	T_J2_J3	0
	T_J2_j4	524
	T_J3_J4	301
	Topple_all	6910
	With 1 failure	5486
	With >1 failure	1424
All modes	All_failures	15152
	With 1 failure	10587
	With 2 failures	2904
	With 3 failures	1415
	With >3 failures	246

multiple failure modes. In the 17% of Area A mapped as unstable slopes, wedge failure is kinematically possible in about 55% of those unstable slopes, topple failure is kinematically possible in about 37% of those unstable slopes and plane failure is kinematically possible in about 8% of those unstable slopes. For plane failure, none of the unstable pixels has more than one plane failure mechanism, but for wedge failure, about 10% of the unstable pixels have more one than one wedge failure mechanism (Table V). For topple failure, about 21% of the unstable pixels has more than one topple failure mechanisms (Table V).

As a validation of the results, all the mapped prominent retrogressive deep-seated rockslides (Dp_rs) and 39 of the 52 mapped shallow translational rockslides (Sh_rs) coincide with pixels modeled to be unstable for certain modes of rock slope failure (Figure 10). The synoptic analysis of kinematical possibility for certain modes of rocks slope failure (Figure 10d) suggest that extensive portions of the terrain Area A are pos-

sibly unstable although no rockslides have been mapped in those portions for the period 1968–2007. However, a large proportion of the areas of 'old and inactive' slides coincide with those possibly unstable slopes where no rockslides in the last four decades have been mapped.

Multi-temporal analysis of rock slope failure possibility in Area A

Because structural discontinuity orientation data are 'static', rock slope instability assessment based solely on such data result in a 'snap-shot' model of possibly unstable slopes (e.g. any map in Figure 10). However, in tectonically active mountainous terrains like the Himalaya, slope modifications or mass-movement processes are a continuous and imminent process (Burbank *et al.*, 1996). Therefore, it can be hypothesized that modeling of spatially-distributed rock slope instability using structural discontinuity orientation data and multi-temporal topographic data may provide useful insights into the temporal evolution of discontinuity-controlled rock slope instabilities. This hypothesis is supported by our earlier analysis of multi-temporal landslide inventories in the study area (Ghosh *et al.*, 2009), which suggest that landslide activities plausibly persisted in the past (i.e. prior to 1968) and such landslide activities continued to the present as confirmed landslide events within the last four decades (1968–2007). Of those events, the events of 1968, 1979, 1993, 1998, 2003 and 2007 were the most devastating. Interviews with local people also indicate that the deep-seated rockslides in Area A (DR1, DR2 and DR3 in Figure 11) have experienced several phases of retrogression during those major landslide events within the last four decades. Our record of DR2 further suggests that, during 1968, initiation points of this particularly larger rockslide were located at much lower elevations (Figure 11) and through repeated retrogressions in the course of time, the slope morphometry of DR2 is considerably changed and now it is a much larger deep-seated rockslide.

In order to explore our hypothesis, therefore, we performed the same spatially-distributed rock slope instability assessment by using the TopoDEM of 1969 in order to map possibly unstable slopes prior to 1969. The result of the kinematical modeling of rock slope instability shows that most of the possibly unstable slopes prior to 1969 coincide with areas of 'old and inactive' slides (Figure 11). Therefore, even though the two DEMs we used for the multi-temporal rock slope instability assessments shown in Figure 11 are based on completely different and incomparable sources of topographic data and, thus, could not be properly constrained, the delineated 'past' and present possibly unstable slopes coincide, respectively, with areas of 'old and inactive' slides and recent rockslides. In addition, the results shown in Figure 11 suggest that the areas of possibly unstable slopes increase from the 'past' to present. Thus, the results of the multi-temporal analysis rock slope instability assessments seem to be realistic, in regard to the knowledge that the area continuously experiences tectonic uplift (Burbank *et al.*, 1996, Wesnousky *et al.,* 1999) such that areas of unstable slopes plausibly increase rather than decrease. However, multi-temporal testing of kinematical possibility of rock slope failure can only be properly justified by using consistent and comparable DEMs in terms of data source and spatial resolution.

Rock slope instability in Area B

Following the same procedure performed for the rock slope instability assessment in Area A, we also identified 10 m ×
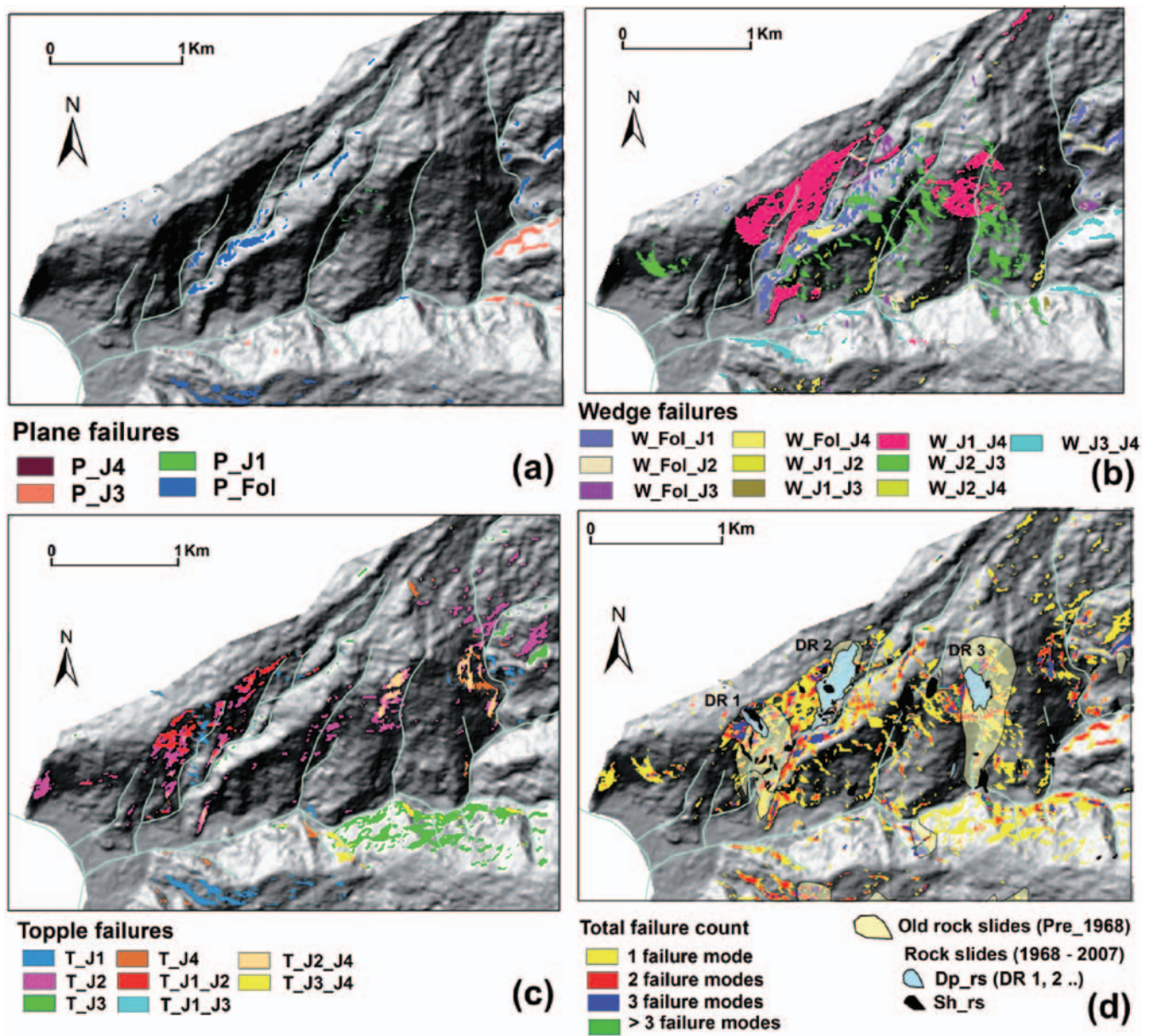
Figure 10. Unstable slopes in Area A [based on CartoDEM of 2006, interpolated map of residual friction angles of discontinuities (Figure 7), and DStMs of orientation data] according to different failure modes and discontinuity-controlled failure mechanisms in Area A (see Table V). (a) Slopes where plane failure is kinematically possible. (b) Slopes where wedge failure is kinematically possible. (c) Slopes where topple failure is kinematically possible. (d) Slopes where at least one failure mode is kinematically possible.

10 m pixels in the entire study area where certain modes of rock slope failures are kinematically possible and their respective discontinuity-controlled failure mechanisms. For Area B, we used the DStMs for the structural domains, the raster map of Φ'_d values, and raster maps of slope and aspect derived from the 10-m resolution CartoDEM of 2006.

The results presented in Table VI and Figure 12 can be summarized as follows. There is possibility for any mode of rock slope failure in about 6·5% of Area B (5·9 km²). In the 6·5% of Area B mapped as unstable slopes, wedge failure is kinematically possible in about 60% of those unstable slopes, topple failure is kinematically possible in 28% of those unstable slopes and plane failure is kinematically possible in 12% of those unstable slopes. For possibility of plane failure mode, failure mechanism P_Fol provides the highest contribution of about 96% to rock slope instability. Of the six identified possible wedge failure mechanisms, prominent contributions to rock slope instability are provided by failure mechanisms

W_J2_J3 (52%), W_Fol_J1 (24%) and W_Fol_J4 (23%). Only eight of the 15 possible topple failure mechanisms could possibly result in topple failures, and the most prominent contribution to rock slope instability is provided by T_J2 (52%). Combining all failure modes together results in about 78% unstable slopes where only one failure mechanism is kinematically possible and in about 22% unstable slopes where more than one failure mechanisms are kinematically possible.

Evaluation of Rock Slope Instability Maps

Our proposed GIS-based methodology for rock slope instability assessment follows the deterministic approach to landslide susceptibility modeling, but it considers only the geometrical relationships between topographic slopes and structural discontinuities in rocks to assess the binary kinematical possibil-
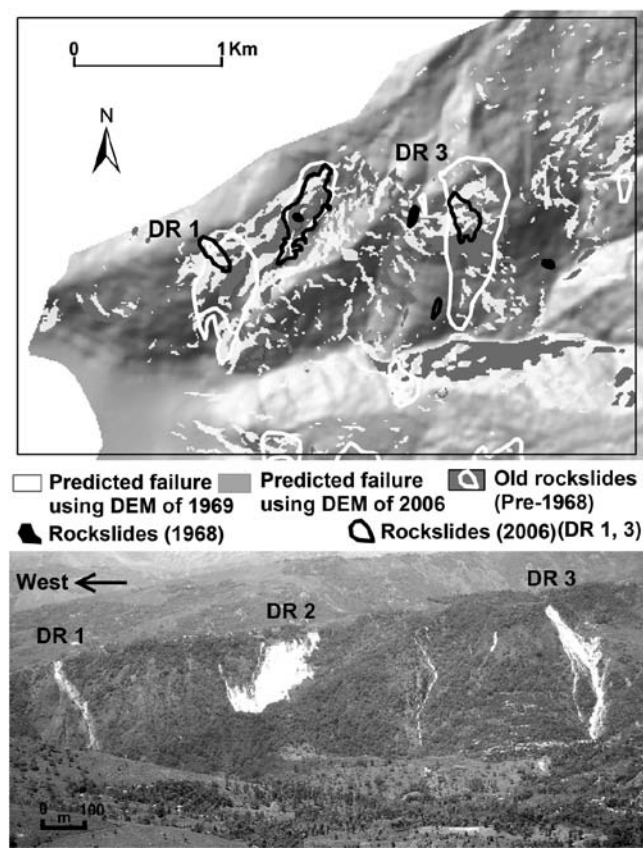
Copyright © 2010 John Wiley & Sons, Ltd.

Earth Surf. Process. Landforms, Vol. **35**, 000–000 (2010)

Figure 11. Unstable slopes in Area A derived by using TopoDEM of 1969 (top figure) and locations of rockslides (bottom photograph, taken in 2006).

ity of certain modes of slope failures. Our rock slope instability assessment maps, therefore, do not represent spatially-varying degrees of likelihood or probability of rockslide occurrence based on a set of known (training) occurrences of rockslides and various causal factors or explanatory variables of rockslides. In addition, according to our discussion in the first two paragraphs in the introduction section and according to the relationships of variables depicted in Equations 1 and 2, which form the bases of our kinematical testing of slope failure, each of our rock slope instability maps is actually a map of multi-variate factors (or multi-evidence) contributing to both increase in shear stress acting on slopes and decrease of shear strength of slope materials. Because there are several other factors of rockslide occurrence that are beyond the scope of this study, each of our rock slope instability maps is, therefore, not a prediction (e.g. probabilistic) map of rockslide occurrence, although they could be used as inputs to predictive mapping of rockslide occurrence. Accordingly, the cross-validation method proposed by Chung and Fabbri (1999) using another set of known (testing) landslide occurrences is not suitable for evaluating our rock slope instability assessment maps. Thus, direct application of the cross-validation method of Chung and Fabbri (1999), using both sets of Dp_rs and Sh_rs as testing rockslides, results in somewhat poor prediction rates of at most 46% in Area A and at most 33% in Area B.

Proper evaluation of slope instability models like those proposed in this paper involves application of comprehensive spatial datasets containing information about slope instabilities locations of open cracks, release places, and actual failure initiation locations, but not entire landslide areas. Unfortunately, such required spatial datasets are currently unavailable. An alternative way to test the efficacy of a rock slope instability

Table VI. Number of pixels where different discontinuity-controlled failure modes and their respective failure mechanisms are kinematically possible in Area B

Failure mode	Failure mechanisms	Number of pixels
Plane	P_fol	8641
	P_J1	11
	P_J2	1
	P_J3	71
	P_J4	290
	Planar_all	8988
	With 1 failure	8962
	With >1 failure	26
Wedge	W_Fol_J1	10604
	W_Fol_J2	0
	W_Fol_J3	0
	W_Fol_J4	9975
	W_J1_J2	100
	W_J1_J3	422
	W_J1_J4	0
	W_J2_J3	23064
	W_J2_j4	1103
	W_J3_J4	3819
	Wedge_all	43492
	With 1 failure	38143
	With >1 failure	5349
Topple	T_Fol	0
	T_J1	4462
	T_J2	10259
	T_J3	2616
	T_J4	2735
	T_Fol_J1	0
	T_Fol_J2	0
	T_Fol_J3	0
	T_Fol_J4	0
	T_J1_J2	1053
	T_J1_J3	525
	T_J1_J4	0
	T_J2_J3	0
	T_J2_j4	503
	T_J3_J4	278
	Topple_all	19756
	With 1 failure	17559
	With >1 failure	2197
All modes	All_failures	59255
	With 1 failure	46218
	With 2 failures	6576
	With 3 failures	5014
	With >3 failures	1447

factor (or evidence) map as a predictor of rockslide occurrence is to characterize and quantify the spatial association of that factor (or evidence) map with a rockslide occurrence map. A positive spatial association between a factor (or evidence) map and a landslide occurrence map implies that the factor map is a good predictor of the landslide occurrence map; otherwise, the factor map is a poor predictor of the landslide occurrence map. Given that any of our rock slope instability maps (*f*) is binary and any of rockslide occurrence maps (*s*) is also binary, we can calculate their Yule's coefficient (Y_c) as follows (cf. Fleiss, 1991; Bonham-Carter, 1994):

$$Y_c = \frac{\sqrt{M_{fs}/M_{\bar{f}s}} - \sqrt{M_{f\bar{s}}/M_{\bar{f}\bar{s}}}}{\sqrt{M_{fs}/M_{\bar{f}s}} + \sqrt{M_{f\bar{s}}/M_{\bar{f}\bar{s}}}} \tag{3}$$

where M_{fs} is area of 'positive match' where both factor and landslides are present, $M_{\bar{f}s}$ is area of 'mismatch' where factor is absent but landslides are present, $M_{f\bar{s}}$ is also area of 'mis-
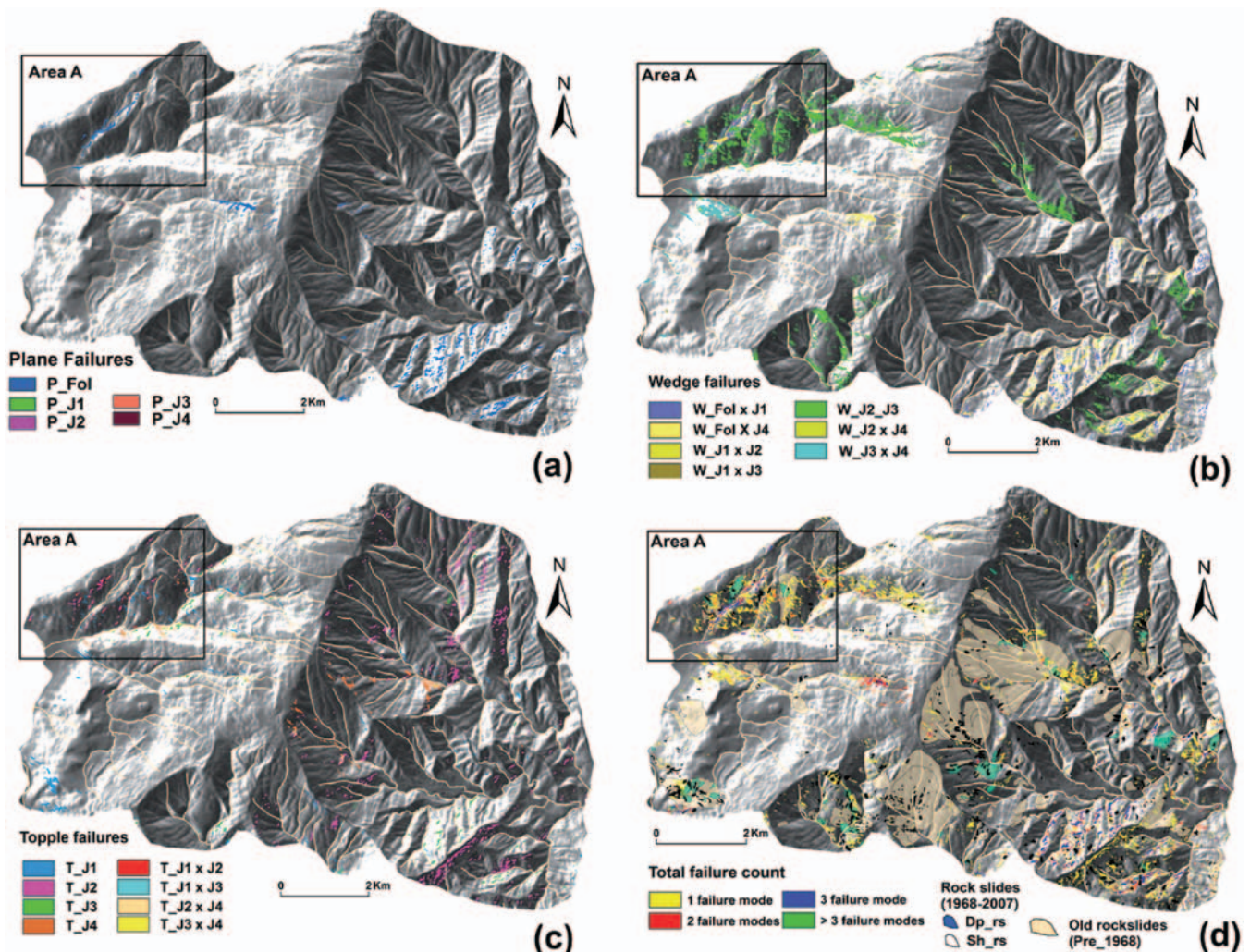
Figure 12. Unstable slopes in Area B [based on CartoDEM of 2006, interpolated map of residual friction angles of discontinuities (Figure 7), and DStMs of orientation data] according to different failure modes and discontinuity-controlled failure mechanisms in Area B (see Table VI). (a) Slopes where plane failure is kinematically possible. (b) Slopes where wedge failure is kinematically possible. (c) Slopes where topple failure is kinematically possible. (d) Slopes where at least one failure mode is kinematically possible.

match' where factor is present but landslides are absent and $M_{\bar{ls}}$ is area of 'negative match' where both factor and landslides are absent. The Y_c ranges in value between −1 and +1, just like the Pearson correlation coefficient. A negative Y_c means negative spatial association, whereas a positive Y_c means positive spatial association. Note that the value of Y_c is based on areal proportions, which are also the bases in spatial conditional probability calculations (cf. Bonham-Carter, 1994). Therefore, in probabilistic terms, a positive Y_c implies that a factor of slope instability increases the likelihood of landslide occurrence, whereas a negative Y_c implies that a factor of slope instability decreases the likelihood of landslide occurrence.

The values of Y_c for each map of slope failure mode (Tables IV and V) calculated against the maps of Sh_rs and Dp_rs are given in Table VII. Following the *t*-test for significance of a correlation coefficient and based on *N* total number of pixels in each of the two test areas, the calculated values of Y_c in Table VII are all significant at 99·9% level. In either Area A or Area B, unstable slopes for plane failure mode have mainly negative spatial associations with known rockslides, implying that, because Y_c is related to conditional probability, occurrence of either Sh_rs or Dp_rs in identified unstable slopes for plane failure mode is unlikely. Likewise, in either Area A or Area B, unstable slopes for wedge and topple failure modes

Table VII. Yule's coefficients of unstable slopes with known rockslides in Areas A and B

Area	Unstable slopes	Sh_rs	Dp_rs
A	Plane failure slopes	−0·047	−0·114
	Wedge failure slopes	0·266	0·450
	Topple failure slopes	0·189	0·322
	All unstable slopes	0·215	0·387
B	Plane failure slopes	0·083	−0·122
	Wedge failure slopes	0·179	0·205
	Topple failure slopes	0·244	0·308
	All unstable slopes	0·216	0·258

have positive spatial associations with either Sh_rs or Dp_rs, implying that, because Y_c is related to conditional probability, occurrence of either Sh_rs or Dp_rs in identified unstable slopes for either wedge or topple failure mode is likely. The results also show that unstable slopes have stronger spatial associations with Dp_rs than with Sh_rs, implying that the different sets structural discontinuities provide stronger structural controls on Dp_rs occurrence than on Sh_rs occurrence. These evaluations of the results are consistent with our field observations of the rockslides in either Area A or Area B.

Scenario-based Slope Instability Assessment

In order to examine conditional failure along pre-existing structural discontinuity planes in areas where slope failure modes are kinematically possible, we attempted to model slope failure susceptibility according to different groundwater saturation scenarios. Based on the Mohr–Coulomb failure criterion, a slope is stable if the critical shear stress (τ_{crit}) acting on potential failure planes is equal to the cohesion (c_d) and frictional resistance acting on those planes, thus:

$$\tau_{crit} = c_d + (\sigma - u)\tan\Phi'_d \qquad (4)$$

where σ is normal stress acting on potential failure planes, u is hydrostatic pressure and Φ'_d is the residual friction angle of the potential failure planes. Conversely, based the Mohr–Coulomb failure criterion, slope failure occurs when τ_{crit} exceeds the right-hand side of Equation 4. Accordingly, pixel-based modeling of lithostatically induced shear stress on structural discontinuities can be performed if orientations of structural discontinuities are known and if orientations and ratios of the three principal deviatoric stresses (σ_1, σ_2 and σ_3) are also known (Günther, 2003; Günther *et al.*, 2004). For slope instability assessment, we considered solely the reduction of σ acting on structural discontinuities due to different hydrostatic pressures (u) (Equation 4). That is because most of the landslide events that occurred in the study area during the period 1968–2007 are rainfall-induced (Ghosh *et al.*, 2009). Thus, all other phenomena that are prevalent in natural conditions and that could reduce σ acting on structural discontinuities, such as earthquake shaking, and reduction of shear strengths, are beyond the scope of the present study.

In order to model the distribution of stress acting on certain structural discontinuities, we applied the concept of reduced stress tensors consisting of four parameters, three for the orientations of the three principal deviatoric stresses (σ_1, σ_2 and σ_3) and one for the ratio of the three principal stresses $R = (\sigma_2 - \sigma_3)/(\sigma_1 - \sigma_3)$ (e.g. Angelier, 1994). Reduced stress tensors are fully equivalent to complete stress tensors in terms of orientations and ratio of three principal stresses. This concept allows computation of shear/normal stress distributions on arbitrary oriented planes of individual terrain elements (e.g. pixels) solely from geometrical parameters in a dimensionless manner, provided that the orientations of the principal stresses are specified for every pixel (Günther, 2003). For simplicity, we considered that, at every pixel, the major principal deviatoric stress (σ_1) is vertical and the least principal stress (σ_3) is horizontal. Thus, at every pixel, the total shear stress and the normal stresses can be estimated by linear up-scaling of the dimensionless principal stresses for certain lithostatic depths based on the following relations

$$\sigma_{vertical} = \rho g h = \sigma_1 \qquad (5)$$

$$\sigma_{horizontal} = \frac{v}{1-v}\sigma_1 = \sigma_3, \text{ and} \qquad (6)$$

$$R(\sigma_1 - \sigma_3) + \sigma_3 = \sigma_2 \qquad (7)$$

where, ρ is rock mass density (in g/cm³); g is acceleration due to gravity (in m/s²), h is lithostatic depth (in meters), v is Poisson's ratio, which can generally be approximated to 0·25, and R (the ratio of the three principal stresses) is by default set to 0·3.

For scenario-based slope instability assessment, we only considered constant model parameters, such as ρ is 2·65 g/cm³ and cohesion is zero because about 95% of the joint planes are smooth. We assumed a lithostatic depth (h) of 20 m

for calculation of σ_1, and three hypothetical saturation conditions ($u = 0$ for 'low' saturation, $u = 0·5$ for 'intermediate' saturation, $u = 1$ for 'full' saturation). The lithostatic depth (h) of 20 m was assumed to incorporate the maximum probable depth-to-failure surface of deep seated rock slides (Dp_rs). We also assume that the orientations of the principal stresses and the structural discontinuity planes do not change within the assumed lithostatic depth. We considered that two extreme saturation conditions because no slope failures have been reported during the dry season in the study area, but during the wet season (June–October) excessive precipitation in Darjeeling Himalaya can result in intermediate to full saturation conditions in many slopes and/or can trigger landslides (Basu and De, 2003).

We performed scenario-based slope instability assessment only for pixels where any discontinuity-controlled failure mechanism is kinematically possible and only in Area A (Table V, Figure 10d). In Figure 13, we illustrate the results of our stress-induced slope instability assessment per failure mode due to different hypothetical saturation conditions. About 18% of the 15 152 pixels where any discontinuity-controlled failure mechanism is kinematically possible become unstable in 'low' saturation condition (Figure 13a). About 66% of the 15 152 pixels where any discontinuity-controlled failure mechanism is kinematically possible become unstable in 'intermediate' saturation condition (Figure 13b). About 91% of the 15 152 pixels where any discontinuity-controlled failure mechanism is kinematically possible become unstable in 'full' saturation condition (Figure 13c).

Thus, the results show clearly and realistically that slope instability increases with increasing level of saturation. To evaluate our scenario-based slope instability maps, we also calculated their Yule's coefficient against the mapped Dp_rs and Sh_rs. The values of Y_c for each map of unstable slopes [per failure mode and per saturation condition (Figure 13)] calculated against the maps of Sh_rs and Dp_rs in Area A are given in Table VIII. Following the *t*-test for significance of a correlation coefficient and based on N total number of pixels in Area A, the calculated values of Y_c in Table VIII are all significant at 99·9% level.

The results show that unstable slopes for plane failure in different saturation conditions have negative spatial associations with known rockslides whereas unstable slopes for either wedge or topple failure in different saturation conditions have positive spatial associations with either Sh_rs or Dp_rs. These results imply that occurrence of either Sh_rs or Dp_rs in identified unstable slopes for plane failure is unlikely in different saturation conditions, whereas occurrence of either Sh_rs or Dp_rs in identified unstable slopes for either wedge or topple failure is likely in different saturation conditions. Moreover, as the saturation condition increases, unstable slopes for wedge failure tend to have increasing positive spatial association with either Sh_rs or Dp_rs, whereas unstable slopes for topple failure tend to have decreasing positive spatial association with either Sh_rs or Dp_rs. These results imply that, as saturation increases, the likelihood or occurrence of either Sh_rs or Dp_rs in identified unstable slopes for wedge failure increases, whereas the likelihood of occurrence of either Sh_rs or Dp_rs in identified unstable slopes for topple failure decreases. The implication of the results for increasing likelihood of wedge failure as saturation increases is explainable because wedge failure would imply high density of different types of structural discontinuities and, therefore, increased permeability of bedrock facilitating water infiltration. The implication of the results for decreasing likelihood of toppling as saturation increases is interesting but rather difficult to explain and, therefore, requires further research. Finally, the indication of
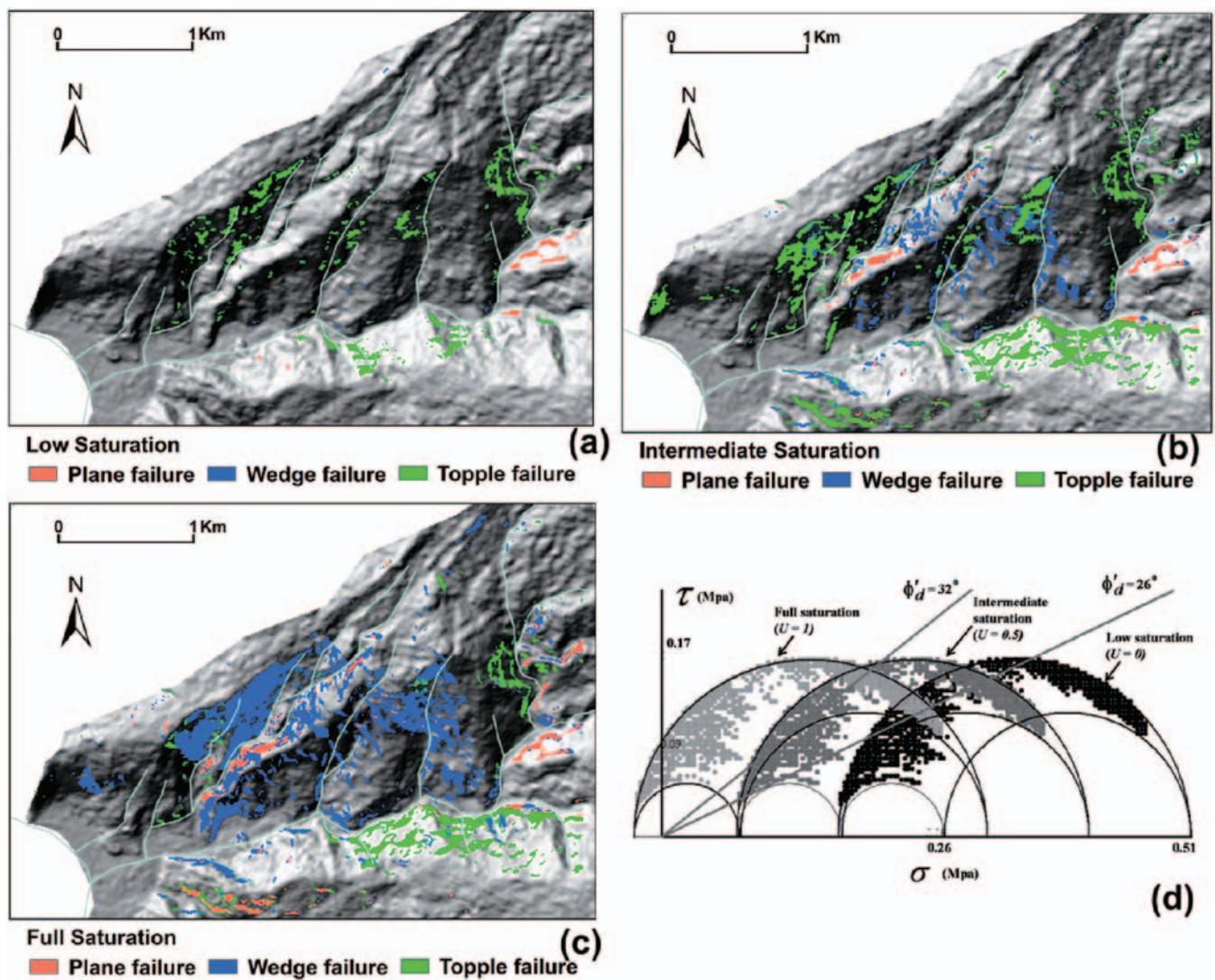
Figure 13. Unstable slopes in Area A based on CartoDEM of 2006, interpolated map of residual friction angles of discontinuities (Figure 7), DStMs of orientation data, and different hypothetical hydrologic conditions. (a) Slopes where different failure modes are kinematically possible in low saturation condition. (b) Slopes where different failure modes are kinematically possible in intermediate saturation condition. (c) Slopes where different failure modes are kinematically possible in full saturation condition. (d) Mohr circle triplets indicating principal stress magnitudes in low, intermediate and full saturation conditions.

Table VIII. Yule's coefficients of unstable slopes (in different saturation conditions) with known rockslides in Area A

Saturation	Unstable slopes	Sh_rs	Dp_rs
Low	Plane failure slopes	−0·274	−0·363
	Wedge failure slopes	0·088	0·337
	Topple failure slopes	0·336	0·384
	All unstable slopes	0·303	0·355
Intermediate	Plane failure slopes	−0·328	−0·614
	Wedge failure slopes	0·247	0·465
	Topple failure slopes	0·228	0·368
	All unstable slopes	0·195	0·344
Full	Plane failure slopes	−0·568	0·595
	Wedge failure slopes	0·282	0·472
	Topple failure slopes	0·140	0·307
	All unstable slopes	0·202	0·406

the results that unstable slopes have stronger spatial associations with Dp_rs than with Sh_rs, implying that the different sets structural discontinuities provide stronger structural controls on Dp_rs occurrence than on Sh_rs occurrence, are con-

sistent with our field observations of the rockslides in Area A (as well as in Area B).

Discussion

The ability of the techniques for assessment of discontinuity-controlled rock slope instability discussed in this paper to characterize the complexity of a structural setting at certain observation scales depend on density and spatial distribution of available point orientation data of structural discontinuities in rocks. Consequently, the quantity and quality of available point orientation data of structural discontinuities in rocks influence (a) the choice of approach to regionalization of those data into continuous DStMs and, consequently, (b) the accuracy of the DStMs. For rock slope instability assessment in small areas where there might be high density and good spatial distribution of point orientation data of structural discontinuities in rocks, as in Area A, spatial interpolation is never completely devoid of any artifact or uncertainty and does not always replicate local structural variations due to incomplete data as a consequence of poor exposure conditions, thick vegetation and/or overburden cover and poor

accessibility in rugged terrains. For rock slope instability assessment in large areas where there might be low density and poor spatial distribution of point orientation data of structural discontinuities in rocks, as in Area B, subdividing the area into smaller and unique domains according to certain structural criteria is intuitive but using the mean of point orientation data of structural discontinuities in every structural domain in order to regionalize such data is an unavoidable oversimplification that could render the results to be meaningless. However, if in Area B (or in large areas) there is high density and good spatial distribution of point orientation data of structural discontinuities in rocks, then delineation of structural domains must still be adopted but the point orientation data must be interpolated as in Area A. Alternatively, probabilistic assessment of discontinuity orientations may be derived from vector statistics of point orientation data, although the main drawback of this the validity of a priori assumption of structural homogeneity.

The techniques for creation of DStMs described here assume that, in every pixel, discontinuity orientation is invariant. This assumption explicitly oversimplifies our rock slope instability assessments whereas in natural conditions it can be observed that structural discontinuities often either disappear or change in orientation very rapidly. Accurate modeling of such natural conditions, however, might be extremely difficult to achieve especially in geo-environments like the Himalayan FTB.

Regionalization of empirically-derived values of (Günther and Thiel, 2009), which are proxies for shearing strengths of structural discontinuities, through spatial interpolation also incurs spatial uncertainties, which could adversely affect results of rock slope instability assessments. An ideal approach is to obtain large number of *in situ* or laboratory test data of shear strength of structural discontinuities at several representative locations in a study area. Obtaining such data for large areas, however, is always costly and extremely time-consuming and, thus, cannot be applied either for timely assessment of rock slope instability. Because carrying out comprehensive geotechnical testing of rock samples for a large study area was beyond the scope of the present research, we had to depend on an interpolated map of proxy data for shearing strength of joints in rocks. This, nonetheless, allowed us to (a) perform rock slope instability assessments according to several possible rock slope failure mechanisms and (b) obtain spatially distributed patterns of kinematically possible discontinuity-controlled slope failure mechanisms in a large area and in a small area and (c) perform multi-temporal analysis of slope instability in a small area.

In both our two test areas, we found that wedge failure is the predominant failure mode followed by toppling and then plane failure, which are consistent with our observations during fieldwork for compiling our landslide inventory. For wedge failures in both test areas, we found that failure mechanisms W_J2_J3, W_J1_J4 and W_Fol_J1 are the most prominent, which make sense because the respective cutting lines of those structural discontinuities have shallow plunges and, thus, have the maximum possibility of being daylighted in moderate to steep slopes. Where the cutting lines of W_J2_J3, W_J1_J4 and W_Fol_J1 have plunges that are steeper than the residual friction angles, they increase the kinematical possibility of slope failure. Following Woodcock's (1977) method to describe fabric shapes of structural orientation data, we obtained k-values of less than one (indicating oblate orientation tensors describing girdle distributions) for all sets of model cutting lines except for Fol_J3 and Fol_J4 for Area A only ($k = 1\cdot8$ and $k = 2\cdot4$ respectively, indicating clustered distributions). This suggests that most wedge failure mechanisms in the study area (Tables V and VI) are predicted by our modeling

approach to produce wedges sliding in widely distributed directions, with the exception of the aforementioned failure mechanisms resulting in wedges mostly sliding to north (Fol_J3, azimuth 1°) and north-northwest (Fol_J4, azimuth 336°) directions. For topple failures in both test areas, we found that kinematical possibility of topple failure is not due to shallow-dipping foliation planes alone but due to wedges formed by foliation planes and all sets of joint planes. This finding is realistic because topple failure is likely to occur only in the presence of steeply-dipping structural discontinuities and steeply-plunging cutting lines of at least two types of structural discontinuities (cf. Goodman and Bray, 1976), such that in both test areas slope failure is highly kinematically possible due to steeply-dipping discontinuity surfaces such as J1, J2 and J3, and steeply-plunging cutting lines such as those of T_J1_J2. For plane failures, we found that failure mechanisms involving foliation planes (P_Fol) are the most prominent, which makes sense because foliations in both two test areas are shallow-dipping and, thus, are likely to be daylighted. The realistic findings from our analyses of kinematical possibility of slope failure indicate the efficacy of the techniques we applied for slope instability assessments at two different spatial scales, which allow us to obtain meaningful insights into different possible failure mechanisms that are involved in both shallow translational rockslides and deep-seated rockslides with the entire study area. For example, it seems that, in either of the two test areas, particular sets of structural discontinuities in rocks provide scale-invariant roles in slope instability. Thus, a quantitative assessment of the scale-invariant role of structural discontinuities in slope instability would be a motivation for further study.

Although rockslides are complex phenomena, in the present research we considered only one vital factor of rock slope instability, which is the geometric relationship between topography, residual friction angles and orientations of structural discontinuities. This consideration is motivated by our belief that rockslides within the entire study area are discontinuity-controlled because the Himalayan FTB is a tectonically active area, although we do not ignore the fact that many devastating landslide events within the entire study area are rainfall-triggered. Therefore, we also attempted to develop scenario-based maps of slope instability by using some arbitrary uniform boundary conditions and assumptions of some global saturation conditions. We acknowledge that our scenario-based assessment of slope instability is hampered by the fact that we do not have a spatially distributed model on groundwater table response to recharge. Therefore, we also acknowledge that our global assumption of a highly pessimistic scenario (i.e. full saturation; Figure 13c) is highly likely only in mostly southerly-facing slopes because they mostly receive significant amounts of monsoon precipitation coming usually from the south. In addition, although we believe that some landslides events within the entire study area are earthquake-triggered but due to lack of suitable data, we were also not able to develop scenario-based maps based on a spatially distributed model of dynamic loading due to earthquake triggering, which could be an important parameter for actual slope instability conditions in a tectonically active geo-environment like the Himalayan FTB. This would be another motivation for further research.

It is also important to state there could be other factors, which are influencing the rockslides in the study area such as changing discontinuity conditions, weathering, local slope saturations, and permeability contrasts. Therefore, further investigation of rock mass and discontinuity properties, methods on their regionalization, and incorporation of such information into similar stability models will definitely improve

Copyright © 2010 John Wiley & Sons, Ltd.

Earth Surf. Process. Landforms, Vol. **35**, 000–000 (2010)

the methods further. Also, a quantitative multivariate assessment of structural evidence layers would be an important issue for future research.

Finally, although our techniques follow deterministic approaches to landslide susceptibility modeling, we have neither considered nor quantified uncertainties in the input data (DEM derivates, structural models, discontinuity shear strengths) and we have not performed or probabilistic analysis of slope instability (e.g. Hack *et al.*, 2003; Jaboyedoff *et al.*, 2004; Park *et al.*, 2005). Accordingly, our slope instability maps (Figures 10, 12 and 13) only indicate binary kinematical possibility of rock slope failure(s). Incorporation of uncertainty analysis of both input data and output information as well as probabilistic analysis in a methodology for rock slope instability assessment would, therefore, certainly be a major motivation for the physically-based rock slope failure modeling. Nevertheless, the evaluations of our slope instability maps (Figures 10, 12 and 13), which are actually maps of multivariate factors (or evidence) contributing to both increase in shear stress acting on slopes and decrease of shear strength of slope materials but they are not prediction maps of rockslide occurrence, consistently indicate that, in both test areas, structural discontinuities are more important controls on deep-seated rockslides than on shallow translational rockslides. These results are realistic and, therefore, suggest that the different techniques adapted in Area A and in Area B in order to assess discontinuity-controlled rock slope instability are non-trivial and could, therefore, be adapted in data-poor situations.

Conclusions

The major conclusions that can be drawn from our study are the following:

- Deterministic assessment of rock slope instability relies heavily on density and spatial distribution of point orientation data of structural discontinuities in rocks.
  - For small areas where there is usually high density and good spatial distribution of point orientation data of structural discontinuities, good DStMs can be obtained via spatial interpolation with structural breaklines.
  - For large areas where there is usually low density and poor spatial distribution of point orientation data of structural discontinuities, good DStMs can be obtained by subdividing the area into structural domains according to meaningful structural criteria and by using the mean of point orientation data in every structural domain.
- An interpolated map of empirically-derived residual friction angles (Φ_d^r) is a useful proxy for a spatially distributed map of shearing strengths of structural discontinuities, which is an important explanatory variable of rock slope instability.
- Within the entire study area
  - individual sets of structural discontinuities (i.e. foliation planes and joint sets) in rocks seem to provide scale-invariant roles in rock slope instability,
  - the predominant mode of slope failure is wedge failure, followed by topple failure and by plane failure,
  - structural discontinuities are more important controls on deep-seated rockslides than on shallow translational rockslides, and
  - rock slope instability increases with increasing levels of water saturation.
- The different techniques adapted in this study in order to assess discontinuity-controlled rock slope instability could be adopted and/or adapted in data-poor situations.

- The slope instability maps obtained in this study are actually maps of multivariate factors contributing to both increase in shear stress acting on slopes and decrease of shear strength of slope materials. They can be used as input maps in probabilistic predictive modeling of landslide susceptibility.

References

Acharya SK, Ray SK. 1977. Geology of Darjeeling-Sikkim Himalaya. *Guide to 4th International Gondwana Symposium*, Calcutta; 25 pp.

Aksoy H, Ercanoglu M. 2007. Fuzzified kinematic analysis of discontinuity-controlled rock slope instabilities. *Engineering Geology* **89**: 206–219.

Aleotti P. 2004. A warning system for rainfall-induced shallow failures. *Engineering Geology* **73**: 247–265.

Anbalagan R. 1992. Landslide hazard evaluation and zonation mapping in mountainous terrain. *Engineering Geology* **32**: 269–277.

Angelier J. 1994. Fault-slip analysis and paleostress reconstructions. In *Continental Deformation*, Hancock PL (ed.). Pergamon: Oxford; 53–100.

Basu SR, De SK. 2003. Causes and consequences of landslides in Darjeeling-Sikkim Himalayas. *Geographia Polonica* **76**: 37–52.

Bieniawski ZT. 1989. *Engineering Rock Mass Classifications*. Wiley: New York; 251 pp.

Bonham-Carter GF. 1994. *Geographic Information Systems for Geoscientists: Modelling with GIS*. Pergamon: Ontario; 398 pp.

Burbank DW, Leland J, Fielding E, Anderson RS, Brozovic N, Reid MR, Duncan C. 1996. Bedrock incision, rock uplift and threshold hillslopes in the northwestern Himalayas. *Nature* **379**: 505–510.

Carrara A. 1999. Use of GIS technology in the prediction and monitoring of landslide hazard. *Natural Hazards* **20**: 117–135.

Chung CJF, Fabbri AG. 1999. Probabilistic prediction models for landslide hazard mapping. *Photogrammetric Engineering and Remote Sensing* **65**: 1389–1399.

Cruden DM. 1989. Limits to common toppling. *Canadian Geotechnical Journal* **26**: 737–742.

Dapporto S, Aleotti P, Casagli N, Polloni G. 2005. Analysis of shallow failures triggered by the 14–16 November 2002 event in the Albaredo valley, Valtellina (northern Italy). *Advances in Geosciences* **2**: 305–308.

De Kemp EA. 1998. Three-dimensional projection of curvilinear geological features through direction cosine interpolation of structural field observations. *Computers & Geosciences* **25**: 269–284.

De Kemp EA. 1999. Visualization of complex geological structures using 3-D Bézier construction tools. *Computers & Geosciences* **25**: 581–597.

Dutta KK. (ed.). 1966. Landslips in Darjeeling and neighbouring hillslopes in June, 1950. *Bulletin of Geological Survey of India* 7–30.

Fleiss JL. 1991. *Statistical Methods for Rates and Proportions*, 2nd edition. John Wiley & Sons: Chichester; 321 pp.

Ghosh S, van Westen CJ, Carranza EJM, Jetten VG. 2009. Generation of event-based landslide inventory maps in a data-scarce environment: case study around Kurseong, Darjeeling district, West Bengal,

Copyright © 2010 John Wiley & Sons, Ltd.

Earth Surf. Process. Landforms, Vol. 35, 000–000 (2010)

India. In Malet JP, Bogaard T (eds). European Centre on Geomorphological Hazards (CERG): Strasbourg; 37–44.

Goodman RE, Bray JW. 1976. Toppling of rock slopes. *Proceedings, Speciality Conference on Rock Engineering for Foundations and Slopes*. American Society of Civil Engineers (ASCE): Boulder, CO.

Günther A. 2003. SLOPEMAP: programs for automated mapping of geometrical and kinematical properties of hard rock hill slopes. *Computers & Geosciences* **29**(7): 865–875.

Günther A, Carstensen A, Pohl W. 2004. Automated sliding susceptibility mapping of rock slopes. *Natural Hazards and Earth System Sciences* **4**: 95–102.

Günther A, Thiel C. 2009. Combined rock slope stability and shallow landslide susceptibility assessment of the Jasmund cliff area (Rügen Island, Germany). *Natural Hazards and Earth System Sciences* **9**: 687–698.

Gupta SK, Saha AK, Arora MK, Kumar A. 1999. Landslide hazard zonation in a part of the Bhagirathi valley, Garhwal Himalayas, using integrated remote sensing – GIS. *Himalyan Geology* **20**: 71–85.

Guzzetti F, Carrara A, Cardinali M, Reichenbach P. 1999. Landslide hazard evaluation: a review of current techniques and their application in a multi-scale study, central Italy. *Geomorphology* **31**: 181–216.

Hack R, Price D, Rengers N. 2003. A new approach to rock slope stability – a probability classification (SSPC). *Bulletin of Engineering Geology and the Environment* **62**: 167–184.

Hoek E, Bray JW. 1981. *Rock Slope Engineering*. The Institution of Mining and Metallurgy: London; 358 pp.

Hubbard M. 1996. Ductile shear as a cause of inverted metamorphism: example from Nepal Himalaya. *Journal of Geology* **194**: 493–499.

Jaboyedoff M, Baillifard F, Philipossian F, Rouiller JD. 2004. Assessing fracture occurrence using 'weighted fracturing density': a step towards estimating rock instability hazard. *Natural Hazards & Earth System Science* **4**: 83–93.

Jaboyedoff M, Couture R, Locat P. 2009. Structural analysis of Turtle Mountain (Alberta) using digital elevation model: toward a progressive failure. *Geomorphology* **103**: 5–16.

Mallet F. 1875. On the geology and mineral resources of the Darjeeling district and the western Duars. *Memoirs of Geological Survey of India* **11**: 1–50.

Matheson GD. 1983. *Rock Stability Assessment in Preliminary Site Investigations – Graphical Methods*, Report 1039. Transport and Road Research Laboratory: Crownthorne.

Meentemeyer RK, Moody A. 2000. Automated mapping of conformity between topographic and geological surfaces. *Computers & Geoscience* **26**: 815–829.

Orr CM. 1996. *Use of Rock Mass Rating (RMR) System in Assessing the Stability of Rock Slopes, Milestones in Rock Mechanics*. Balkema: Leiden; 159–172.

Pantelidis L. 2009. Rock slope stability assessment through rock mass classification systems. *International Journal of Rock Mechanics and Mining Sciences* **46**: 315–325.

Park HJ, West TR, Woo I. 2005. Probabilistic analysis of rock slope stability and random properties of discontinuity parameters, Interstate Highway 40, Western North Carolina, USA. *Engineering Geology* **79**: 230–250.

Romana M (ed.). 1985. *A Geomechanics Classification for Slopes: Slope Mass Rating. Comprehensive Rock Engineering*. Pergamon Press: Oxford; 575–600.

Roy S, Mandal N. 2009. Modes of hill-slope failure under overburden loads: insights from physical and numerical models. *Tectonophysics* **473**: 324–340.

Searle MP, Szule AG. 2005. Channel flow and ductile extrusion of the high Himalayan slab – the Kanchenjunga – Darjeeling profile, Sikkim Himalaya. *Journal of Asian Earth Sciences* **25**: 173–185.

Selby MJ. 1993. *Hillslope Materials and Processes*. Oxford University Press: Oxford; 451 pp.

Serafim JL, Pereira JP (eds). 1983. Considerations on the geomechanical classification of Bieniawski. In *Proceedings, International Symposium of Engineering Geology and Underground Construction*. Balkema: Rotterdam.

Sinha-Roy S. 1982. Himalayan main central thrust and its implication for Himalayan inverted metamorphism. *Tectonophysics* **84**: 197–224.

Sitar N, MacLaughlin MM, Doolin DM. 2005. Influence of kinematics on landslide mobility and failure mode. *Journal of Geotechnical and Geoenvironmental Engineering* **131**: 716–728.

Soja R, Starkel L. 2007. Extreme rainfall in eastern Himalaya and southern slope of Meghalaya plateau and their geomorphologic impacts. *Gemorphology* **84**: 170–180.

Swan ARH, Sandilands M. 1995. *Introduction to Geological Data Analysis*. Blackwell: Oxford; 446 pp.

UNESCO-WP/WLI. 1993. A suggested method for describing the activity of a landslide. *Bulletin of the International Association of Engineering Geology* **47**: 53–57.

Varnes DJ. 1978. Slope movements types and processes. In *Landslides: Analysis and Control*, Schuster RL, Krizek RL (eds), Special Report 176. Transportation Research Board, National Academy of Sciences: Washington, DC; 11–33.

Wagner A, Leite E, Olivier R. 1988. Rock and debris-slides risk mapping in Nepal – a user-friendly PC system for risk mapping. In *Proceedings of the 5th International Symposium on Landslides*, Bonnard C (ed.). Balkema: Rotterdam; 1251–1258.

Wallbrecher E. 1986. *Tektonische und Gefügeanalytische Arbeitsweisen*. Enke-Verlag: Stuttgart.

Wesnousky SG, Kumar S, Mohindra R, Thakur VC. 1999. Uplift and convergence along the Himalayan frontal thrust of India. *Tectonics* **18**: 967–976.

Woodcock NH. 1977. Specification of fabric shapes using an eigenvalue method. *Geological Society of America Bulletin* **88**: 1231–1236.

AUTHOR QUERY-FORM

Dear Author:

   During the preparation of your manuscript for publication, the questions listed below have arisen. Please attend to these matters and return this form with your proof.

Many thanks for your assistance.

Query References	Query	Remarks
1.	AU: Please provide title of book.	